Tectonophysics 745 (2018) 245–263

Contents lists available at ScienceDirect

Tectonophysics

journal homepage: www.elsevier.com/locate/tecto

Crustal earthquakes in the Cook Inlet and Susitna region of southern Alaska

Vipul Silwal[a,*], Carl Tape[a], Anthony Lomax[b]

[a] Geophysical Institute, University of Alaska, Fairbanks, USA
[b] ALomax Scientific, Mouans-Sartoux, France

ARTICLE INFO

Keywords:
Cook Inlet
Susitna
Moment tensor
Earthquakes

ABSTRACT

Several large ($M \geq 6$) earthquakes have occurred in the vicinity of Anchorage, Alaska, within the past century. The presence of the underlying subducting Pacific plate makes it difficult to determine the origin of these older earthquakes as either crustal, slab, or the subduction plate interface. We perform a seismological study of historical and modern earthquakes within the Cook Inlet and Susitna region, west of Anchorage. We first estimate hypocenters for historical large earthquakes in order to assess their likelihood of origin as crustal, slab, or plate interface. We then examine modern crustal seismicity to better understand the style of faulting and the location of active structures, including within (and beneath) the Cook Inlet and Susitna basins. We perform double-couple moment tensor inversions using high frequency body waves (1–10 Hz) for small to moderate ($M \geq 2.5$) crustal earthquakes (depth $\leq$ 30 km) occurring from 2007 to 2017. Our misfit function combines both waveforms differences as well as first-motion polarities in order to obtain reliable moment tensor solutions. The three focus regions—Beluga, upper Cook Inlet, and Susitna—exhibit predominantly thrust mechanisms for crustal earthquakes, indicating an overall compressive regime within the crust that is approximately consistent with the direction of plate convergence. Mechanisms within upper Cook Inlet have strike directions aligned with active anticlines previously identified in Cook Inlet from active-source seismic data. Our catalog of moment tensors is helpful for identifying and characterizing subsurface faults from seismic lineaments and from faults inferred from subsurface images from active-source seismic data.

1. Introduction

Modern tectonic activity in south-central Alaska is governed primarily by the northwestern subduction of the Pacific plate beneath the North America plate (Fig. 1). This setting is one of the most seismically active regions in the world, having produced the M_w9.2 1964 earthquake. It includes pervasive earthquakes in the subducting slab, down to depths of 200 km, as well as crustal seismicity spanning a broad zone of intraplate deformation (Fig. 2) (Page et al., 1991; Bird, 2003). Many of the earthquakes—both large and small—are not clearly associated with any faults that appear on published surface geological maps. With improved locations of earthquakes and determination of the style of faulting from these earthquakes, we can better characterize the extent, and activity, of faults in the region. Here, we perform a seismological study of a tectonically complex region of south-central Alaska to improve our understanding of active tectonics and seismic hazards in the region.

The Pacific plate subducts to the northwest under south-central Alaska (Fig. 1a). Attached to the Pacific plate to the east is the Yakutat microplate, identified as an oceanic plateau, that is colliding and subducting beneath Alaska (Plafker et al., 1978; Eberhart-Phillips et al., 2006; Christeson et al., 2010). The subducting Pacific/Yakutat plate is interpreted to be responsible for the extremely shallow angle of subduction (< 5°), far inland, as well as for the noteworthy lack of volcanism in the Susitna basin and Talkeetna Mountains, in a magmatic gap between the Aleutian volcanic arc on the west and the Wrangell volcanic field on the east (Fig. 1a) (Eberhart-Phillips et al., 2006; Rondenay et al., 2010).

We focus on a lowlands region marked by the presence of two major sedimentary basins (Figs. 1b and 3): the Cook Inlet basin south of the Castle Mountain fault, and the Susitna basin north of the fault (Fig. 1b). We refer to this region, which is outlined in Fig. 1b, as the Cook Inlet and Susitna region. The Susitna basin and the smaller, Peters Hill (or Yentna) basin (Haeussler, 2008; Haeussler et al., 2017b), are within the Susitna lowlands, which is outlined in Fig. 1b by Kirschner (1988). The Susitna lowlands and the Cook Inlet basin (Fig. 3) are surrounded by mountains (Fig. 1b): the Talkeetna Mountains to the east, the Alaska Range to the northwest, the Tordrillo Mountains to the west, and the Kenai Mountains to the south.

The Cook Inlet and Susitna region spans the western margin of the

* Corresponding author.
E-mail addresses: vsilwal@alaska.edu (V. Silwal), ctape@alaska.edu (C. Tape), anthony@alomax.net (A. Lomax).

https://doi.org/10.1016/j.tecto.2018.08.013
Received 13 June 2018; Received in revised form 14 August 2018; Accepted 16 August 2018
Available online 29 August 2018

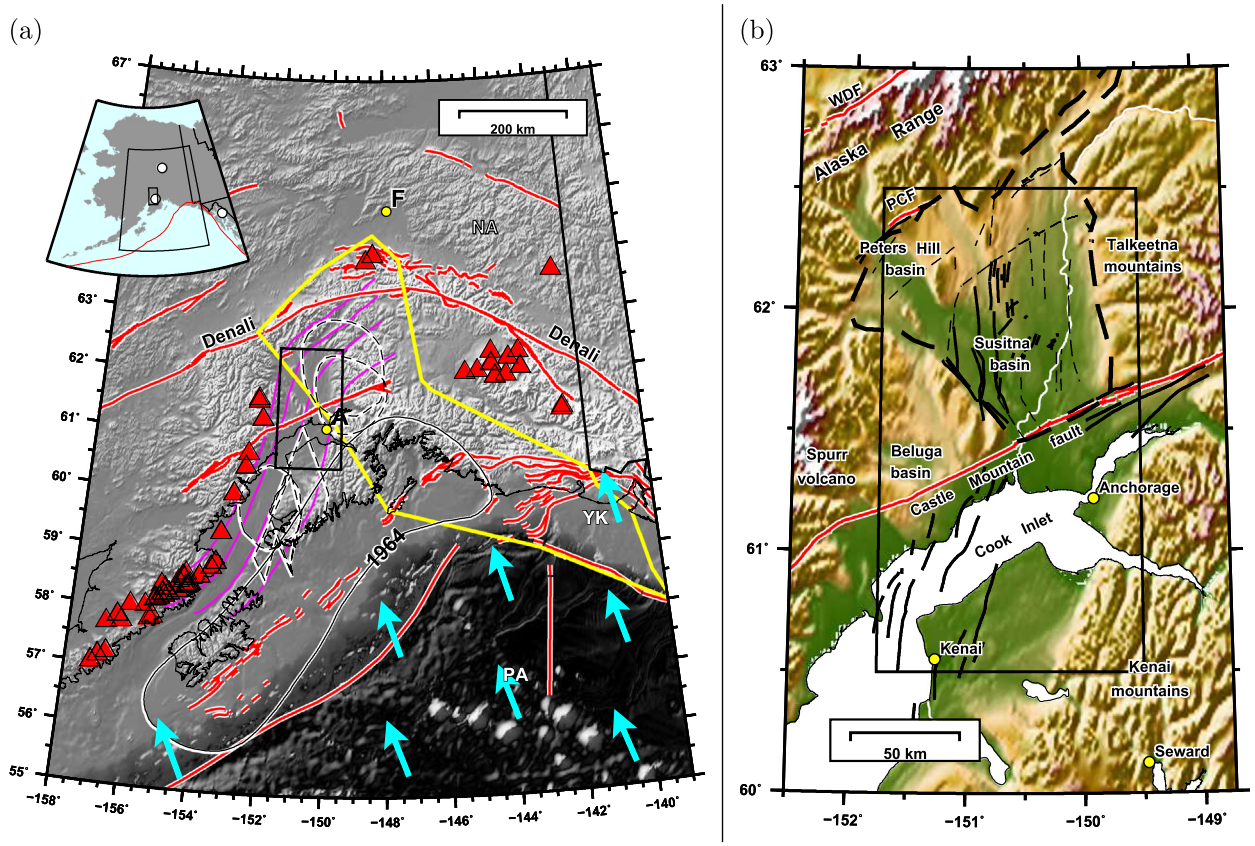

Fig. 1. (a) Active tectonic setting of the Aleutian–Alaskan subduction zone, south-central Alaska. The rectangle in the middle shows the main study region. Cyan arrows shows the plate vectors for the subducting Pacific plate (PA) under the North American plate (NA) (Bird, 2003). Red lines denote active faults (Koehler et al., 2012). Magenta curves are the 40 km, 60 km, 80 km, and 100 km contours of the subduction interface, i.e.,, the top of the Pacific plate (Li et al., 2013). Yellow bounded region denotes the surface and subsurface extent of the Yakutat block (YK) (Eberhart-Phillips et al., 2006). Red triangles represent active volcanoes. Black dashed lines are inferred slow slip events from various sources (Ohta et al., 2006; Wei et al., 2012; Fu and Freymueller, 2013; Li et al., 2016). Also marked is the aftershock zone of the 1964 M_w9.2 earthquake. Labeled cities: Anchorage (A) and Fairbanks (F). (b) Physiographic map of the Cook Inlet and Susitna region, south-central Alaska. Active faults are plotted in red and include Castle Mountain, Pass Creek (PCF), and the western Denali fault (WDF) at upper left (Koehler et al., 2012). Cook Inlet sedimentary basin underlies Cook Inlet and the western Kenai Peninsula (Shellenbaum et al., 2010) (Fig. 3). North of the Castle Mountain fault are three sedimentary basins: Beluga, Susitna, and Peters Hill. Active folds in Cook Inlet basin (Koehler et al., 2012) are marked in black. Other faults in Susitna basin also marked in black are obtained from Haeussler et al. (2017b) and Shah et al. (2015) (Fig. S1). The thick black dashed line denotes the boundary of Susitna lowlands Kirschner (1988). (For interpretation of the references to color in this figure legend, the reader is referred to the web version of this article.)

Pacific/Yakutat plate (Fig. 1a) and contains several notable tectonic elements. Contours of the depth to the top of the subducting Pacific plate (i.e., the subduction interface) (Li et al., 2013) show a clear kink from a westward-dipping slab to a northwestern-dipping slab (Ratchkovski and Hansen, 2002) (Fig. 1a). The subduction interface ranges from a depth of 40 km in the southeast, beneath the Kenai Peninsula, to a depth of 100 km in the northwest, beneath the Alaska Range. The southeast corner of the region also marks the approximate downdip extent of the 1964 M_w9.2 earthquake (Fig. 1a) (Davies et al., 1981; Ichinose et al., 2007). Slow slip and tectonic tremor have been identified on the deeper sections of the subduction interface, from about 40 km to 80 km (Ohta et al., 2006; Wei et al., 2012; Fu and Freymueller, 2013; Li et al., 2016). The crustal thickness inferred from receiver functions is ~30 km in the northern region (Veenstra et al., 2006), implying that these deeper slow slip events would arise from contact with subcrustal mantle.

The dynamics of underlying subduction provide context for characterizing crustal structures and crustal earthquakes, which are the target of this study. Within the Cook Inlet and Susitna region are two active faults in the publication of Koehler et al. (2012): the Pass Creek fault and the Castle Mountain fault. The earliest description of the Pass Creek fault (PCF) appears in Capps (1913), who reported "over 2000 feet" (p. 31) of displacement across the fault. Using interferometric synthetic aperture radar (IFSAR) elevation data, Haeussler et al. (2017b) inferred the PCF to be a northwest dipping normal fault and that it "appears likely that the scarp is a result of at least several surface-rupturing earthquakes" (p. 1471). They estimated the fault has a slip-rate of ~0.5 mm/yr and has the potential of producing a M6.9 ± 0.3 earthquake if the complete 37 km of the fault plane ruptured. Koehler and Carver (2018) discussed a possible interpretation for the Pass Creek fault as "north-directed backthrusting and hanging wall extension above a blind, north-dipping master thrust" (p. 23).

The Castle Mountain–Lake Clark fault system extends 500 km from Lake Clark in the southwest to the Talkeetna Mountains in the northeast (Grantz, 1966). The fault has been interpreted as a right-lateral strike-slip fault based on geological features (Grantz, 1966; Haeussler and Saltus, 2004; Trop et al., 2005; Willis et al., 2007; Haeussler and Saltus, 2011). Two modern earthquakes, each well-recorded by regional stations, provide support for the Castle Mountain fault—or at least the eastern portion—as a right-lateral strike-slip fault. These earthquakes occurred just east of the Cook Inlet and Susitna region, as 1984-08-14 M_w5.8 (depth 15 km) and 1996-11-11 M_l4.6 (depth 17 km). A detailed study of the 1984 earthquake was presented in Lahr et al. (1986); this was the largest earthquake on the Castle Mountain–Lake Clark fault system within the past 40 years (Dziewonski et al., 1981; Ekström et al.,

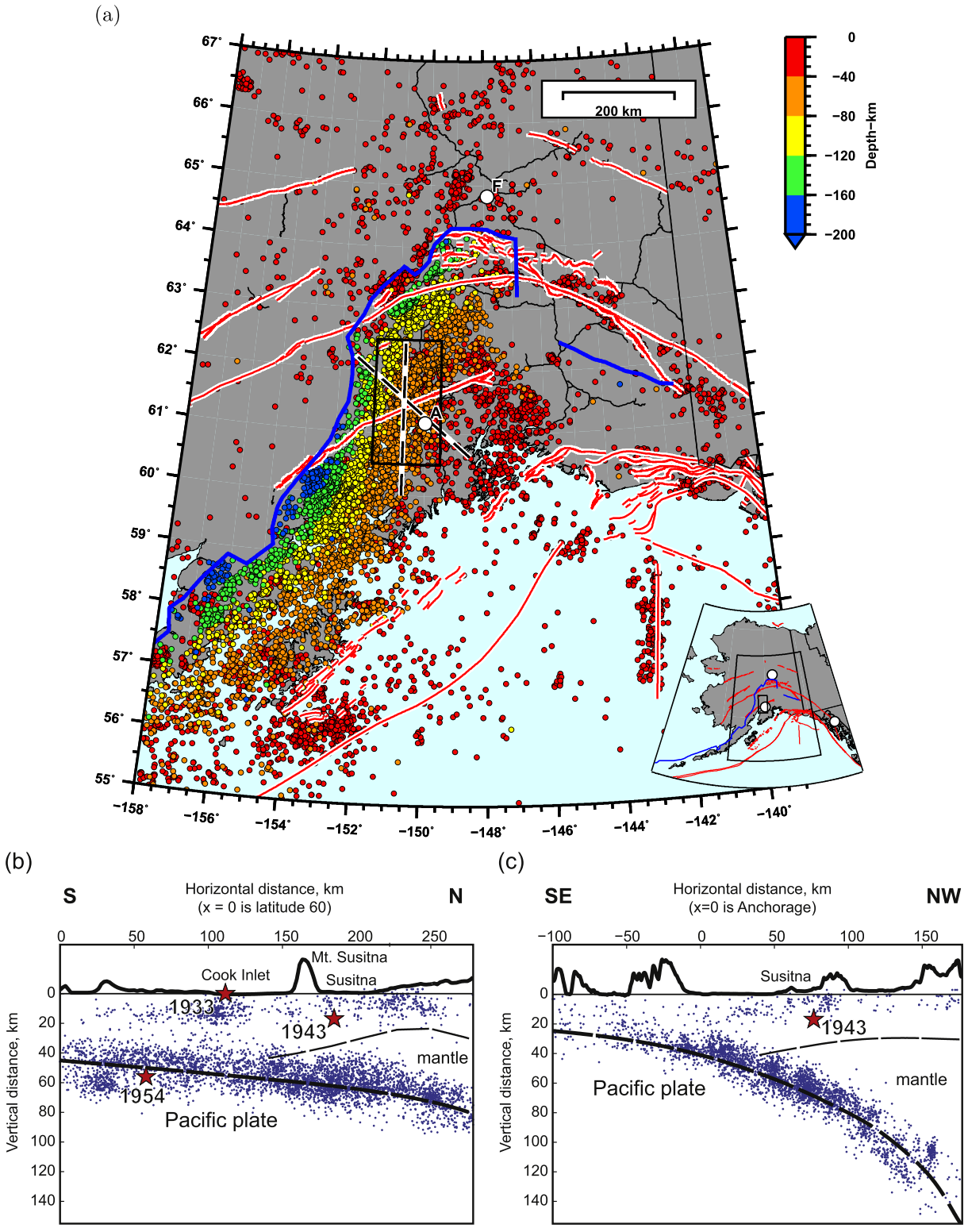

Fig. 2. Seismicity in south-central Alaska. (a) Alaska Earthquake Center (AEC) catalog: $M_w \geq 2$, 1990-01-01 to 2017-01-01, colored by depth. The box, containing Anchorage (A), is the focus region of this study; the two profiles are shown in (b) and (c). The red lines are the active faults from Koehler et al. (2012). The blue line is the lateral extent of slab seismicity, digitized from the full AEC catalog. (b) S–N cross-section of (a) along the longitude line of − 150.75°, from latitude 60° to 62.5°. Seismicity within 20 km of the profile is shown. Three large earthquakes of interest are projected onto the profile: 1933 M_w6.78, 1943 M_w7.34, and 1954 M_w6.36; the hypocenters are estimated from NonLinLoc. Geometric boundaries shown are the subduction interface (Li et al., 2013), the Moho (Wang and Tape, 2014), and topography (Amante and Eakins, 2009) exaggerated by a factor of 20. (c) SE–NW cross-section of (a) between Anchorage (x = 0 km) and the 1943 earthquake. (For interpretation of the references to color in this figure legend, the reader is referred to the web version of this article.)

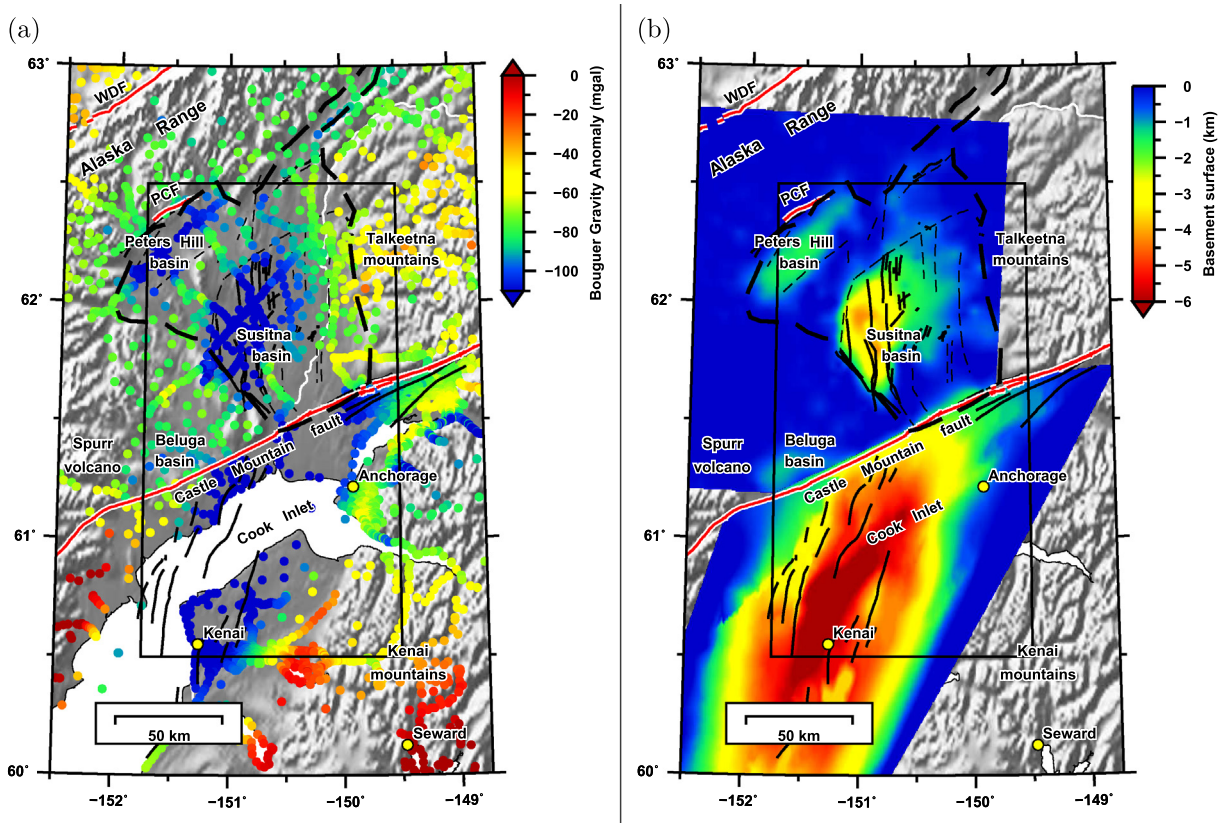

Fig. 3. Gravity data and estimated basement depths for the Cook Inlet and Susitna region; see physiographic map in Fig. 1b for comparison. Faults and folds plotted include active faults (Koehler et al., 2012), active folds in Cook Inlet (Haeussler and Saltus, 2011; Koehler et al., 2012), and faults in the Susitna basin (Lewis et al., 2015; Haeussler et al., 2017b). (a) Bouguer gravity data (Saltus et al., 2016). (b) Maps of depth to base of Cenozoic strata in Cook Inlet basin (Shellenbaum et al., 2010), as well as base of Cenozoic strata in Susitna basin (Wilson et al., 2009), Peters Hill basin, and Beluga basin (Stanley et al., 2013). The dashed outline is the Susitna lowlands region of Kirschner (1988) and Meyer (2005).

2012).

Recent analyses of the Castle Mountain fault have documented geomorphic features (e.g., scarps) consistent with reverse slip across the fault, as well as a lack of definitive lateral offset indicators (Koehler and Carver, 2018). The part of the CMF that extends across the Susitna lowlands is the only part of the fault that shows evidence of Holocene displacement, based on geomorphic evidence (Koehler et al., 2012). This activity is supported by paleoseismic evidence. Haeussler et al. (2002) used data from nine trenches along the fault near Houston, Alaska. They identified four major earthquakes in the past 2800 years, indicating a recurrence interval of ~700 years. Trenching results from Koehler et al. (2015) suggested recurrence intervals closer to thousands of years. The two largest historical earthquakes in the region, in 1933 and 1943, appear to have occurred near, but not on, the fault (Doser and Brown, 2001). Additional faults and folds, besides Pass Creek fault and Castle Mountain fault, have been inferred from potential field data or identified within 3D active-source seismic data in Cook Inlet basin (Magoon et al., 1976; Plafker et al., 1994; Haeussler et al., 2000; Bruhn and Haeussler, 2006; Haeussler and Saltus, 2011) and Susitna basin (Lewis et al., 2015; Shah et al., 2015; Haeussler et al., 2017b) (Fig. 1b).

We conduct a seismological study that spans three different methods and three sets of earthquakes in the Cook Inlet and Susitna region (Table 1). First, in Section 2 we estimate the hypocenters of the largest earthquakes ($M_w \geq 5.8$) that have occurred since the start of the instrumental era in 1904 (Gutenberg and Richter, 1954). We use globally recorded arrival times of P and S waves, in addition to traveltime predictions in a spherically symmetric Earth model, within a probabilistic inversion for hypocenter and origin time. Second, in Section 3 we use P waveforms and first-motion polarities to estimate focal mechanisms for crustal earthquakes $M_w \geq 2.5$. This procedure is challenging on account of the lack of large earthquakes that are available. Third, in Section 4 we relocate seismicity ($M \geq 1.5$, 1990–2017) using arrival time data and a double-difference relocation algorithm (Waldhauser and Ellsworth, 2000). The results from these three analyses reveal a predominance of thrust faulting in the crust, consistent with structural inferences from subsurface images, but differing from the strike-slip mechanisms previously estimated from the large historical earthquakes. Widespread seismicity and different styles of faulting provide challenges for characterizing different scenarios for future large earthquakes in this region.

2. Hypocenter estimation of historical earthquakes

At least 12 major earthquakes ($M_w \geq 5.8$) have occurred in the Cook Inlet and Susitna region since the start of the instrumental era in 1904. Table 2 summarizes previous publications of the magnitudes for these earthquakes. For larger earthquakes we use the Global Centroid Moment Tensor (GCMT) catalog (Dziewonski et al., 1981; Ekström et al., 2012) for events since 1976 and the ISC-GEM catalog (Storchak et al., 2013; International Seismological Centre, 2018) for events before 1976. The ISC-GEM catalog provides relocated hypocenters (Engdahl et al., 1998; Bondár and Storchak, 2011) and magnitude estimates (Giacomo et al., 2015). In recent years, it has expanded its coverage of historical earthquakes to lower magnitudes. Doser and colleagues have estimated hypocenters, magnitudes, and mechanisms for many historical earthquakes in south-central Alaska (Doser and Brown, 2001; Flores and Doser, 2005; Doser, 2005; Doser, 2006).

Depth estimates of the hypocenters and of the subduction interface

Table 1
Earthquake selection for three target subregions and for the full region. N_e is the number of earthquakes analyzed in each region for a particular method.

Region	Longitude		Latitude		Method	N_e	Max depth	Min mag	Date range
	Min (°)	Max (°)	Min (°)	Max (°)			(km)		
Beluga region	−151.50	−151.10	61.25	61.90	Moment tensor	9	30	M_l2.5	2007-08-15 2017-01-01
Upper Cook Inlet region	−151.50	−150.60	60.60	61.25	Moment tensor	22	30	M_l2.5	2007-08-15 2017-01-01
Susitna region	−151.10	−149.90	61.50	62.50	Moment tensor	22	30	M_l3.0	2007-08-15 2017-01-01
Cook Inlet and Susitna region	−151.75	−149.50	60.50	62.50	Historical	12	200	M_w5.8	1904-01-01 2017-01-01
	−152.00	−149.00	60.50	62.50	Double difference	5726	30	M_l1.5	1990-01-01 2017-01-01

provide a starting point for interpreting the earthquakes as either crustal, interface, or intraslab. Table 3 reveals a mix of crustal and intraslab (or interface) earthquakes. Interestingly, the occurrence of earthquakes in the crust versus the slab appears to have changed with time, as shown in Fig. 4. Prior to 1950 most earthquakes were crustal; after 1950 all four earthquakes were in the slab. This pattern was previously noted (Doser and Brown, 2001) and is apparent over a larger region. Doser and Brown (2001) speculated that stress changes from the 1964 M_w9.2 earthquake were responsible for the shift from crustal to slab earthquakes.

We use a nonlinear probabilistic approach to estimate the hypocenters of the 11 pre-1976 earthquakes $M_w \geq 5.8$ in the region (Table 2). The code, NonLinLoc, uses an efficient global sampling algorithm to obtain an estimate of the probability density function (pdf) in 3D space for the hypocenter location (Lomax et al., 2000). The pdf (and the likelihood) is computed using the misfit between the observed and theoretical arrival times for teleseismic stations. Theoretical travel times are computed for a spherical earth with the ak135 velocity model (Kennett et al., 1995) using the TauP Toolkit (Crotwell et al., 1999). Recorded arrival times are obtained from the International Seismological Centre (International Seismological Centre, 2015).

Our full results for all 11 historical earthquakes are presented in Lomax et al. (2018); next we highlight three of the largest earthquakes.

2.1. The 1933, 1943, and 1954 earthquakes

We present results from three $M_w > 6$ earthquakes in the Cook Inlet and Susitna region: 1933-04-27 M_w6.8, 1943-11-03 M_w7.3, and 1954-10-03 M_w6.4 (Table 2). These earthquakes were widely felt across south-central Alaska, including Kodiak, to the southwest, and at least as far north as Fairbanks, which is about 400 km from the epicenters. Appendix A summarizes felt reports of these earthquakes. The 1933 earthquake toppled telegraph lines around Anchorage, broke storefront windows in Anchorage, and shook houses off foundations in Old Tyonek. The 1954 earthquake produced minor landslides over the highway, damaged a section of railroad, and damaged structures in Anchorage and the western Kenai Peninsula. Although having the largest magnitude of the three earthquakes, the 1943 earthquake did not lead to any reported damage in the region. By comparison, the maximum shaking intensities in Anchorage—which is approximately equidistant from the three earthquakes—were Modified Mercalli Intensity scale (MMI; Wood and Neumann, 1931) 6 (1933), MMI 5 (1943), and MMI 8 (1954) (Appendix A; Brockman et al., 1988). These discrepancies could arise from differences in source-to-site distances, from influences of 3D structure on ground motion, from source effects (radiation pattern or directivity), and from possible inconsistencies in the MMI values (e.g., are the MMI values from the same place in Anchorage?).

The seismicity cross sections in Fig. 2b–c provide context for these three earthquakes. The plots show our maximum likelihood (MLL) hypocenters for the three earthquakes in the context of modern seismicity and estimated subsurface interfaces (subduction and Moho). From these results alone, it appears that the 1933 and 1943 earthquakes are crustal, while the 1954 earthquake was likely intraslab, though we cannot rule out the subduction interface as a possibility (Table 3). We discuss this further in Section 5.3.

Station coverage and traveltime residuals for our MLL hypocenters (and origin times) are shown in Fig. 5. The solution to the relocation problem is a posterior probability density function that can be conveniently represented by samples—the posterior hypocenters—of the distribution (Tarantola, 2005). Fig. 6 shows our posterior epicenters for the three earthquakes. These 'clouds' of posterior epicenters convey the uncertainty associated with the epicenter estimation; in our cases, the clouds are approximately 30 km by 40 km. For each posterior

Table 2
Earthquakes $M \geq 5.8$ in the Cook Inlet and Susitna region (Table 1) of south-central Alaska since the start of the instrumental era in 1904. The events are selected from the ISC-GEM catalog (before 1976-01-01) and GCMT catalog (after 1976-01-01). Depth estimates are listed in Table 3. ISCG = ISC-GEM 5.0 (Storchak et al., 2013), GCMT = Global Centroid Moment Tensor catalog (Dziewonski et al., 1981; Ekström et al., 2012). NA means that the earthquake was outside the time interval of a particular study.

Origin time	Longitude	Latitude	Ref.	Mag. M_w	Ref.	GR (Gutenberg and Richter, 1954) M	Abe (Abe, 1981) M_s, m_b	EV (Engdahl et al., 2002) M_w	DB (Doser and Brown, 2001) M_w
1933-04-27 02:36:07	−151.06	61.10	ISCG	6.78	ISCG	7.0	6.9, 7.1	6.90	7.0
1933-06-12 15:23:41	−151.35	61.23	ISCG	5.82	ISCG	–	–	–	–
1933-06-13 22:19:51	−151.67	61.22	ISCG	5.97	ISCG	6.25	–	–	–
1933-06-19 18:47:46	−151.03	61.39	ISCG	5.85	ISCG	6.0	–	–	–
1934-06-18 09:13:52	−151.40	60.72	ISCG	5.97	ISCG	6.75	–	6.60	6.1
1936-10-23 06:24:21	−151.01	61.17	ISCG	6.82	ISCG	–	–	–	–
1941-07-30 01:51:29	−150.97	60.90	ISCG	6.39	ISCG	6.25	–	–	6.3
1943-11-03 14:32:20	−151.00	61.79	ISCG	7.34	ISCG	7.3	7.4, 7.1	7.20	7.0
1954-10-03 11:18:48	−150.39	60.65	ISCG	6.36	ISCG	NA	–	–	6.6
1974-12-29 18:25:01	−150.58	61.59	ISCG	5.92	ISCG	NA	–	–	NA
1975-01-01 03:55:13	−149.82	61.90	ISCG	5.92	ISCG	NA	–	7.40	NA
1991-05-01 07:18:46	−151.42	62.47	GCMT	6.30	GCMT	NA	NA	6.2	NA

Table 3
Estimated depths, with uncertainties, for the earthquakes in Table 2. Depths are listed in km below sea level. The depths from NonLinLoc (NLL) are for the maximum likelihood, and the uncertainty value is $\sqrt{covZZ}$, where *covZZ* can be found in the NLL output files in Lomax et al. (2018). See also Fig. 7 for examples of depth distributions of all posterior hypocenters. The right three columns list the vertical distance from the ISC-GEM epicenter to the subduction interface, for three different interface models. Events marked as * are likely slab events. For the Engdahl catalog, DEQ means that depth is a free parameter, and FEQ means that depth is fixed based on independent information.

	NLL (this study)	GR (Gutenberg and Richter, 1954)	DB (Doser and Brown, 2001)	EV (Engdahl et al., 2002)	ISCG (Storchak et al., 2013)	JB10 (Jadamec and Billen, 2010)	H12 (Hayes et al., 2012)	L13 (Li et al., 2013)
1933-04-27	0.33 ± 5	0	9 ± 4	35 (FEQ)	15 ± 4	54	68	63
1933-06-12	0.65 ± 20	0	–	–	15 ± 9	71	77	73
1933-06-13	12.71 ± 4	0	–	–	15 ± 9	85	87	82
1933-06-19	16.29 ± 6	0	–	–	15 ± 7	64	71	66
1934-06-18*	49.20 ± 4	80	76 ± 10	50 (DEQ)	60 ± 9	63	72	66
1936-10-23	0.33 ± 4	–	–	–	15 ± 14	56	68	63
1941-07-30	0.33 ± 6	0	–	–	35 ± 14	49	64	59
1943-11-03	17.27 ± 3	0	27 ± 4	35 (FEQ)	15 ± 4	73	75	71
1954-10-03*	55.88 ± 2	N/A	60 ± 10	64	62 ± 5	40	52	45
1974-12-29*	68.10 ± 4	N/A	N/A	–	65 ± 5	56	64	57
1975-01-01*	64.03 ± 3	N/A	N/A	–	63 ± 5	43	57	48
		GCMT	AEC					
1991-05-01*		118	115	114 (DEQ)	113 ± 5	123	110	100

hypocenter we calculate its vertical distance to the subduction interface, and these differences are then plotted as histograms in the bottom row of Fig. 7. These distributions provide critical uncertainties for the interpretation of the earthquakes as crustal, subduction interface, or intraslab. For example, the estimated hypocenter depth shown in Fig. 7c (bottom) is consistent with an intraslab origin for the 1954 earthquake (However, note that we do not have uncertainties for the subduction geometry models, including the one we have chosen to use.) (Li et al., 2013).

3. Moment tensor inversions for modern crustal earthquakes

Recorded seismograms can be used to characterize the style of faulting for an earthquake by using the estimation method of moment tensor inversion. A double couple moment tensor is a 3 × 3 symmetric matrix M whose eigenvalues are $\mathbf{\Lambda} = (\lambda,0,-\lambda)$. The seismic moment of a moment tensor is given by $M_0 = \|M\|/\sqrt{2} = \|\mathbf{\Lambda}\|/\sqrt{2}$, so for a double couple, $M_0 = \lambda$. We are concerned with estimating the magnitude and orientation of the moment tensor. The strike, dip, and rake angles define the moment tensor orientation, as well as one of the two possible fault planes. The moment tensor orientation can be described as a 'fault-plane solution' or 'focal mechanism' or 'source mechanism'; these terms do not encompass the seismic moment (or magnitude). Seismologists represent double-couple moment tensors by plotting the sign of the radial component of the displacement field at the source, then projecting it onto the lower hemisphere. The two-colored pattern is a four-quadrant sphere that resembles a beachball; we use the term beachball when referring to the plotting symbol.

Three catalogs of moment tensors are summarized in Fig. 8: (a) Doser and Brown (2001): large $M_w > 6$ historical (pre-1964) earthquakes; (b) the GCMT catalog (Dziewonski et al., 1981; Ekström et al., 2012): post-1976 earthquakes, predominantly $M_w > 5.3$; (c) crustal earthquakes from the Alaska Earthquake Center fault-plane catalog: predominantly $M_l > 3$. We also considered the focal mechanism catalog of Li et al. (2013), which includes 117 earthquakes over a one-year period of the MOOS deployment (2007–8). Almost all of these earthquakes are within the slab or to the southeast of our focus region.

Within the Cook Inlet and Susitna region, we observe two historical crustal earthquakes (1933, 1943) and zero crustal earthquakes since 1976 (GCMT: Dziewonski et al., 1981; Ekström et al., 2012). There is one event in the GCMT catalog that is ≤ 30 km depth, plotted as a red beachball near Anchorage in Fig. 8b. The depth is listed as 15 km in the GCMT catalog, but the Alaska Earthquake Center (AEC) earthquake catalog, using all available regional data, lists 31 km for the depth, which would likely be an intraslab origin (not crustal) for the earthquake. The GCMT magnitude of M_w5.3 is near the completeness level for the catalog, which indicates that there is limited global data for estimating the moment tensor. This might explain the large discrepancy between the moment tensor from GCMT and the one from the Alaska Earthquake Center, as shown in Fig. 6.

Focal mechanisms for crustal earthquakes since 1990 are available from Alaska Earthquake Center. The mechanisms are estimated from first-motion polarities, and they vary widely across the region. Our primary motivation was to use enhanced methods, including waveforms, and enhanced station coverage from the past decade, to estimate moment tensors.

3.1. Event selection for moment tensor inversions

We consider earthquakes in the Cook Inlet and Susitna region shallower than 30 km and occurring between 2007-08-15 and 2017-01-01. From the spatial distribution of crustal seismicity (Fig. S11), we identified three subregions to select events for moment tensor inversions: Beluga region, upper Cook Inlet region, and Susitna region (Table 1 and Fig. S9). The time period of event selection, 2007–2017, spans two seismic experiments in the region: MOOS (2007–2009) (Li

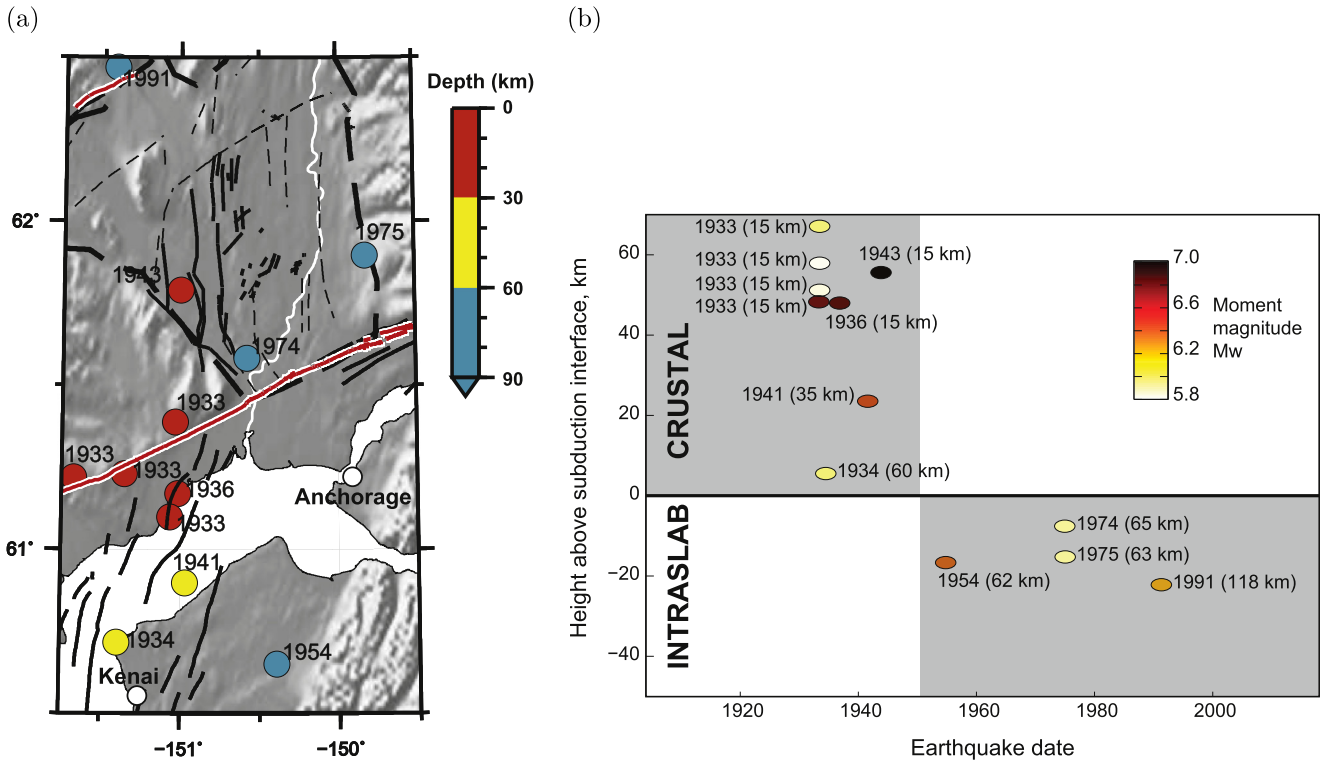

Fig. 4. All 12 major earthquakes ($M_w \geq 5.8$) in the Cook Inlet and Susitna region (see Table 1) Earthquakes are selected from the ISC-GEM catalog for the time interval 1904-01-01 to 2017-01-01. (a) Map showing epicenters, colored by depth. (b) Plot of height above subduction interface (Li et al., 2013) (Fig. 1a) as a function of origin time, for the 12 earthquakes in (a). The checkered shading at the year of 1950 accentuates the pattern of early crustal earthquakes and later (more recent) intraslab earthquakes.

et al., 2013; Abers and Christensen, 2006) and SALMON (2015–2017) (Tape et al., 2017; Tape et al., 2015) and also includes new stations from the EarthScope Transportable Array (TA) in Alaska (2014–2019). Station coverage is a primary factor on the reliability of our moment tensor solutions. Events in 2010, following the end of MOOS, have poor station coverage. Events starting in 2015 have the best coverage due to SALMON and TA networks.

We selected 53 events for moment tensor inversions: 9 from the Beluga region, 22 from the upper Cook Inlet region, and 22 from the Susitna region. Hypocenters and origin times were obtained from the AEC catalog. These were fixed for the moment tensor inversions. Analyst-reviewed P arrival times and polarities were used for stations in the permanent network (AK, AT, AV). For stations in temporary networks (MOOS, SALMON, TA), we picked the P arrival times and assigned polarities.

3.2. Moment tensor inversion method

Estimating a moment tensor for an earthquake involves comparing observed waveforms with synthetic waveforms calculated for an assumed moment tensor for an assumed model of Earth structure. We use the same layered seismic velocity model used by the Alaska Earthquake Center for moment tensor inversions and for locating earthquakes; see Table S1 of Silwal and Tape (2016). We use the 'cut-and-paste' approach to estimate moment tensors for earthquakes (Zhao and Helmberger, 1994; Zhu and Helmberger, 1996; Zhu and Rivera, 2002). In this approach, each three-component seismogram is cut into two body wave windows and three surface wave windows. Different bandpass filters are applied to the body waves and surface waves. The same procedures are applied to synthetic seismograms, which are then quantitatively compared with the recorded seismograms, via a misfit function. As demonstrated in Silwal and Tape (2016), the choices within the misfit function can have a significant impact on the estimated best-fitting moment tensor. Our previous studies (Silwal and Tape, 2016; Alvizuri and Tape, 2016) employed a simplified treatment of first-motion polarities that is generalized here.

Within the grid-search moment tensor inversion, the synthetic seismograms are aligned with the observed seismograms by applying time shifts to the synthetic waveforms that minimize the misfit between synthetic and observed waveforms. In many cases, this minimization can result in time shifts that are unreasonable, based on comparisons with a larger set of measurements. In these cases of cycle skipping, the synthetic waveforms are aligned on the wrong portion of the observed waveforms. The challenges of cycle-skipping and time shifts have been discussed previously (Alvizuri et al., 2018; Alvizuri and Tape, 2016). In our study, we specify the observed P onset times, which effectively eliminates the need for time shifts.

Fig. 9 shows a moment tensor inversion result for one of 22 crustal earthquakes in the Susitna region. Its relatively large magnitude (M_w4.2) allows us to use surface waves, in addition to body waves. For all the other events, only P waves (and P polarities) were used. The example shows the basic approach to comparing recorded waveforms (black) with synthetic waveforms (red) generated using a layered Earth model and a moment tensor source. Significant differences in shapes between data and synthetics are attributed to complexities in 3D Earth structure that are not modeled by the synthetics. For this event, the recorded waveforms to the southwest are influenced by Cook Inlet basin, as well as by Susitna basin from the source region. Some of these differences in structure between our assumed 1D model and real 3D Earth structure are encapsulated by the time shift maps shown in Fig. 9.

3.3. Misfit function

Small earthquakes ($M_w < 3.5$) do not produce large signals at low frequencies. Therefore we are forced to use higher frequency waveforms, which are sensitive to 3D structural heterogeneities. Most

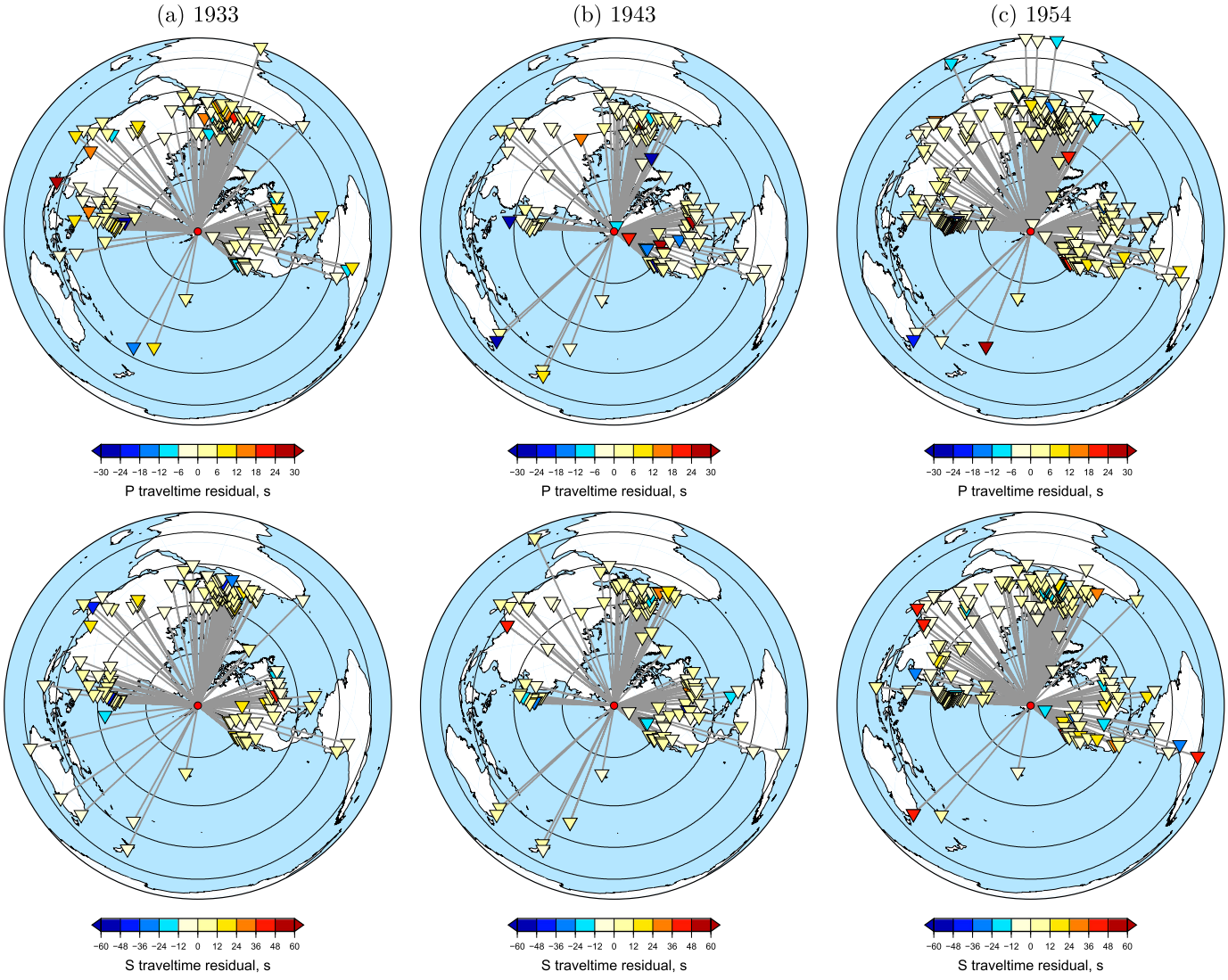

Fig. 5. Station coverage for P arrival times (top) and S arrival times (bottom) used in estimating the epicenters for the 1933, 1943, and 1954 Alaska earthquakes. The maximum likelihood epicenter for each earthquake is marked by red circle at the center. The arrival times of the phases were obtained from ISC (International Seismological Centre, 2015), and the magnitudes listed are from the ISC-GEM catalog (Table 2). The stations are marked by inverted triangles and colored by the difference between the ISC arrival time and synthetic obtained using the ak135 velocity model (Kennett et al., 1995). Circles show epicentral distances of $\Delta = 30^{\circ}$, 60°, 90°, 120°, and 150°. The posterior epicenters for each earthquake are shown in Fig. 6. For details of the results, see Lomax et al. (2018). (a) 1933 M_w6.78 earthquake. There are 174 P arrival times and 158 S arrival times recorded by 179 stations. (b) 1943 M_w7.34 earthquake. There are 137 P arrival times and 136 S arrival times recorded by 137 stations. (c) 1954 M_w6.36 earthquake. There are 346 P arrival times and 223 S arrival times recorded by 263 stations. (For interpretation of the references to color in this figure legend, the reader is referred to the web version of this article.)

regional networks do not have enough stations to capture the detailed effects of 3D structure on the wavefield. As used in previous studies (Chiang et al., 2014; Ford et al., 2012; Guilhem et al., 2014; Wéber, 2018), first-motion polarity measurements (i.e., up or down) can be used to stabilize the waveform misfit function. Below we define our misfit function that combines waveforms differences and polarity differences.

The L1-norm waveform misfit is given by

$$\Phi_w(M) = \sum_{j=1}^{N_s} \sum_{i=1}^{5} [(\mathbf{u}_{ij} - \mathbf{s}_{ij}(M))^T \mathbf{W}_{ij} (\mathbf{u}_{ij} - \mathbf{s}_{ij}(M))]^{1/2} \quad (1)$$

where N_s is the number of stations used, i is the window index for a seismogram, j is the station index for an event, $\mathbf{u}$ is a discretized recorded seismogram, $\mathbf{s}(M)$ is a discretized synthetic seismogram for moment tensor M, $\mathbf{W}_{ij}$ is a square weighting matrix with the same dimension as the number of time points. As discussed in Section S1, we choose $\mathbf{W}_{ij}$ to be a constant-valued diagonal matrix with a weight factor that takes into account the duration of the time window, the width of the bandpass, and an optional user-specified weight. Recent approaches have considered non-diagonal weighting matrices based on estimated noise at each station (Mustać and Tkalčić, 2016, 2017; Stähler and Sigloch, 2016).

The polarity misfit is given by

$$\Phi_p(M) = \frac{1}{2} \sum_{j=1}^{N_p} |p_j - t_j(M)| \quad (2)$$

where p is the observed polarity, t is the theoretical polarity for the moment tensor M, and N_p is the number of stations at which first-motion polarity is picked. p and t can either be $+1$ (up) or -1(down). Considering the $1/2$ factor, the polarity misfit for a station is either 0 or 1, and the allowable values for $\Phi_p(M)$ are 0,1,…,N_p.

The total misfit is a weighted sum of the normalized waveform and polarity misfit

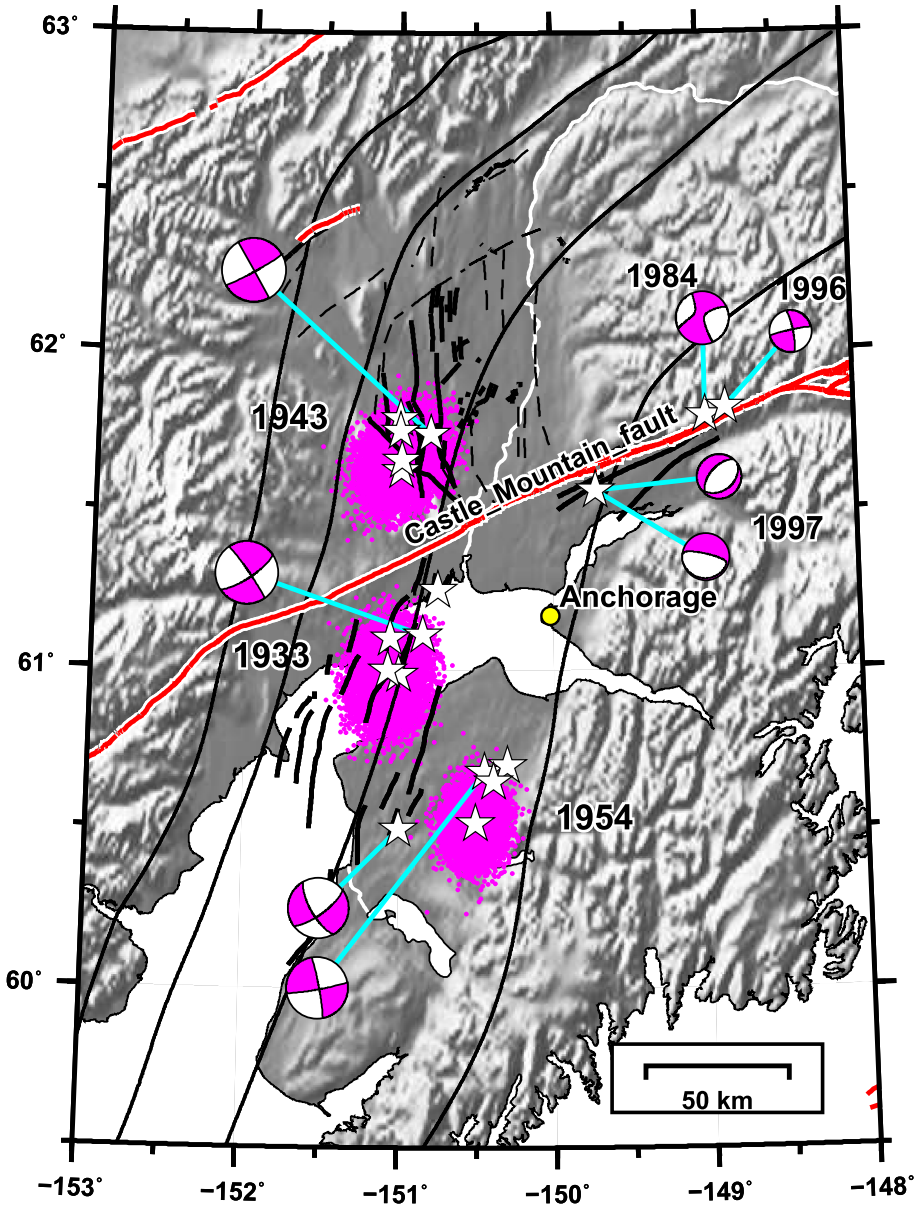

Fig. 6. Estimated epicenters for the 1933, 1943, and 1954 earthquakes; see Lomax et al. (2018) for details. Each cloud of colored dots represents the posterior epicenters, which are centered on a maximum likelihood epicenter (star). Other stars show epicenter estimates from other studies (Table S1: Doser and Brown (2001), Engdahl et al. (2002), Gutenberg and Richter (1954), Storchak et al. (2013); see also Fig. 11). See Fig. 7 for information regarding the depths of the posterior samples relative to the underlying subduction interface. Also shown are active faults and folds (Koehler et al., 2012; Haeussler et al., 2017b) and contours of the subduction interface (i.e., the top of the subducting Pacific plate) at 40 km, 60 km, 80 km, and 100 km (Li et al., 2013). The beachballs show source mechanisms for 1933 (Doser and Brown, 2001), 1943 (Doser and Brown, 2001), 1954 (Doser and Brown, 2001; Wickens and Hodgson, 1967), 1984 (Dziewonski et al., 1981), 1996 (AEC), and 1997 (AEC, Dziewonski et al., 1981). The 1984, 1996, and 1997 epicenters are from the AEC catalog.

$$\Phi(M) = h(N_s)\left(m\,\frac{\Phi_p(M)}{N_p} + (1-m)\,\frac{\Phi_w(M)}{||\mathbf{u}||_{L1}}\right) \quad (3)$$

where the waveform misfit normalization $||\mathbf{u}||_{L1}$ is same as given in Eq. 7 of Silwal and Tape (2016), m is the weight given to the polarity misfit, and $h(N_s)$ is the station reward factor (see Section S1). Fig. 10 shows the impact of using different weights for the polarity misfit on moment tensor solution. The Supporting Information includes text and figures to illustrate the roles of different variables in the misfit function. This misfit function was also used in Alvizuri et al. (2018) and Alvizuri and Tape (in press) for full moment tensor inversions.

3.4. Results

Our moment tensor inversion results for 53 crustal earthquakes in the three subregions (Table 1) are presented in Fig. 11, in Tables S2–S4, and in Silwal (2018). The subregions exhibit predominantly thrust earthquake mechanisms that are consistent with the plate convergence direction of 339° (N21W) (Bird, 2003). Specifically, the T axes of the mechanisms are near vertical, and the P axes of the mechanisms are near horizontal and point in the northwest direction of plate convergence.

In Fig. 12, we compare our moment tensor results, which use P waveforms and first-motion polarities, with a catalog of mechanisms (AECfp) produced by the Alaska Earthquake Center that uses first-motion polarities only (fpfit: Reasenberg and Oppenheimer, 1985). For the time period 2007-08-15 to 2017-01-01 and depths ≤ 30 km, the AECfp catalog contains 46 earthquakes, 26 of which were examined in our study. The additional earthquakes in the AEC catalog were ones that were either not within our three subregions or were excluded by us due to low signal-to-noise levels for waveforms (Section 3.1). Therefore the comparison in Fig. 12 is between a set of 53 moment tensors derived from P waveforms and a set of 46 derived from P polarities. The result in Fig. 12a, which includes 27 that are not in (b), is a more coherent pattern of thrust faulting, whereas Fig. 12b shows predominantly strike-slip faulting. This suggests that the inclusion of waveforms, as in our study, may help discriminate among strike-slip and thrust mechanisms in cases where P polarities alone cannot isolate the mechanism. Specifically, the moment tensor for a north-striking thrust fault dipping 45° (west or east) can be rotated 90° about its P-axis; this will result in a strike-slip moment tensor that is significantly overlapping with the

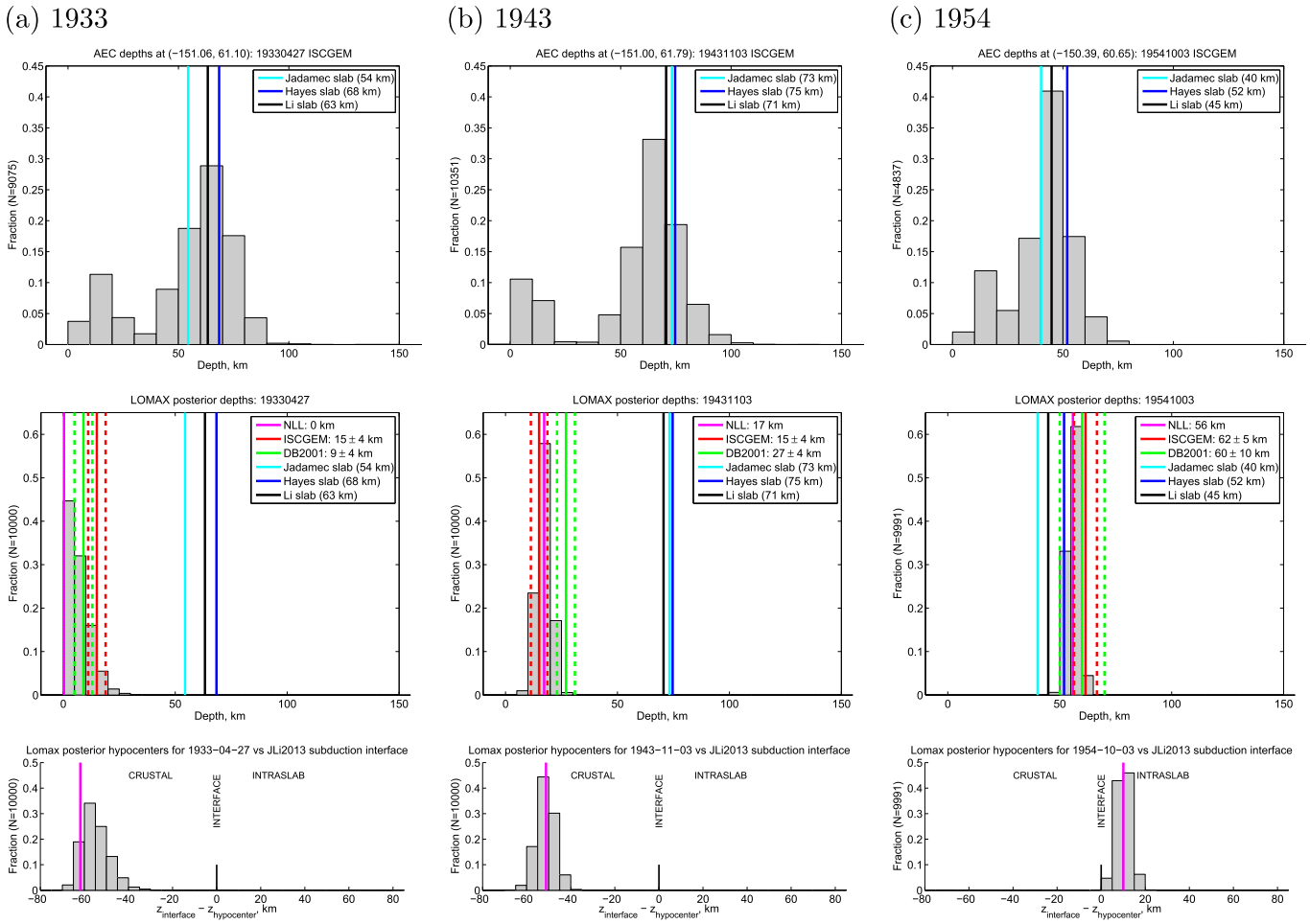

Fig. 7. Estimated depth to subduction interface for three historical earthquakes. Each hypocentral estimation using NonLinLoc provides a cloud of posterior hypocenters; see Fig. 6 for a map view. For each posterior hypocenter we evaluate the vertical distance to the subduction interface models of Jadamec and Billen (2010) (cyan), Hayes et al., 2012 (blue), and Li et al. (2013) (black). (a) 1933-04-27 M_w6.8 earthquake. (top) Distribution of depths of modern microseismicity ($M \geq 0$, 2000–2018) whose epicenters are within a 40 km of the ISC-GEM epicenter. (middle) Distribution of depths of posterior hypocenters. Also shown are our maximum-likelihood estimate from NonLinLoc (magenta) and the depth estimates, with uncertainties, from ISC-GEM (Storchak et al., 2013) (red) and DB2001 (Doser and Brown, 2001) (green). (bottom) Distribution of vertical distances between our posterior hypocenters and the underlying subduction interface from Li et al. (2013). Distributions to the left favor a crustal interpretation for the earthquake; distributions to the right favor an intraslab interpretation. (b) 1943-11-03 M_w7.3 earthquake. (c) 1954-10-03 M_w6.4 earthquake. (For interpretation of the references to color in this figure legend, the reader is referred to the web version of this article.)

original moment tensor (as quantified by $\omega = \angle(M_1,M_2) = 60^\circ$, which is much less than the maximum of 180°). Although the mechanisms look different, they are not easily constrained by seismic data, and a formal assessment of uncertainties could elucidate this point (Silwal and Tape, 2016). Of course, better station coverage would also help discriminate between the strike-slip and thrust mechanisms. By examining small, shallow earthquakes, we are unlikely to have the ray path coverage near the center of the focal sphere. For shallow events, the upward ray paths cover a small region of the Earth's surface, where we are unlikely to have a station. For small events, the downward ray paths often have too-small of signal-to-noise ratios by the time they reach distant stations. Station coverage for the source mechanisms is best viewed in the beachball plots in Silwal (2018).

4. Hypocenter relocation of modern crustal seismicity

We apply the double-difference hypocenter relocation method of Waldhauser and Ellsworth (2000) to crustal seismicity in the Cook Inlet and Susitna region. The double difference method relies on minimizing the difference between observed and theoretical travel-times for pairs of earthquakes at each station. The method, especially when used in conjunction with waveform cross correlations, has been effective in collapsing diffuse clouds of seismicity onto strikingly sharp fault-like features; meanwhile other diffuse clouds remain diffuse (Hauksson and Shearer, 2005; Shearer et al., 2005). The changes in the locations are also used to reduce the systematic errors due to the model, which could be used to improve the tomography models (Zhang and Thurber, 2003).

Our work expands on the results of Ratchkovsky et al. (1998), who relocated crustal earthquakes with $ml > 2.0$ and depths $\leq$ 50 km in southern Alaska occurring during 1988–1996 using the joint hypocenter determination (JHD) method (Douglas, 1967). They classified their results into five regions, one of which coincides with our target region: “Shallow North American intraplate earthquakes (0–25 km) located to the west of 149° W” (p. 96). Their results revealed diffuse seismicity within the crust.

We used a much larger data set, spanning from 1990-01-01 to 2017-01-01, and a more robust double-difference hypocenter relocation method (Waldhauser and Ellsworth, 2000). We used crustal events (depth $\leq$ 30 km) with $M_l \geq 1.5$ occurring between 1990-01-01 and 2017-01-01 (Table 1). With these selection criteria, we started with 5726 events from the AEC catalog. The final relocated catalog, after removing 35 (depth > 40 km) events, contained 4748 earthquakes. The changes between the initial hypocenter and final hypocenter are displayed in Figs. S14 and S13. The mean change in epicenter is about

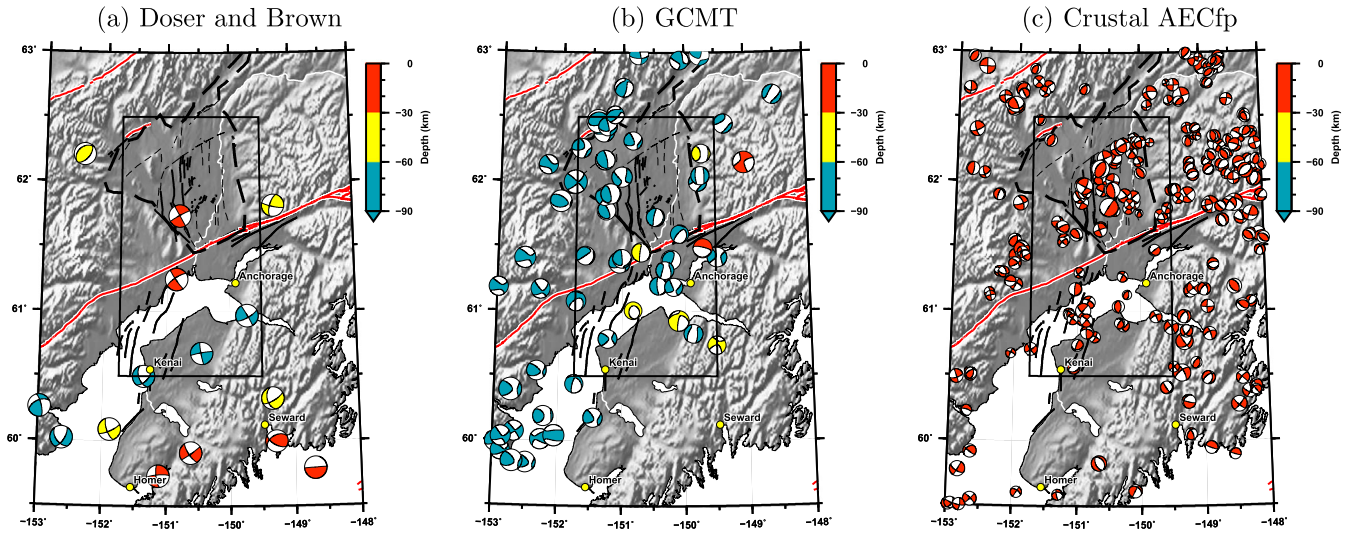

Fig. 8. Moment tensor solutions from previous studies. (a) Major historic events (1920–1964), from Doser and Brown (2001). The three earthquakes near longitude − 150° are, from north to south, the 1943, 1933, and 1954 earthquakes. (b) All events from the GCMT catalog, 1976–2017 (Dziewonski et al., 1981; Ekström et al., 2012). (c) All crustal (depth ≤ 30 km) events (1990-01-01 to 2017-01-01) from the Alaska Earthquake Center fault-plane catalog. These focal mechanisms are derived from P polarity observations. See Section 2 for more information on major historic events. See Fig. 11 for our new moment tensor solutions. (For interpretation of the references to color in this figure, the reader is referred to the web version of this article.)

5 km and the standard deviation of depth changes is about 6 km.

In general, after relocation the diffuse seismicity remains diffuse (Fig. 13). Similar results were obtained for relocations in the Los Angeles basin by Hauksson and Shearer (2005). Hauksson and Shearer (2005) explained the diffuse hypocenters as an effect of complex 3D brittle structure with interlaced strike-slip faults and thrust faults. The main lineament in our study region, within the Beluga region, is rotated toward a N-S alignment after relocation (Fig. 13). Future efforts using new stations and waveform cross-correlation measurements could improve our results.

5. Discussion

Here, we summarize our seismological results in the context of previous work within the three regions of interest (Table 1). We then discuss implications for active faults and larger earthquakes in the region.

5.1. Structures and active tectonics in the Cook Inlet and Susitna region

5.1.1. Beluga region

The Beluga region (Fig. 11a) is physiographically marked by a triangular-shaped feature which we describe as the Beluga "interlowland region" (BILR), after Saltus et al. (2016). The BILR comprises four small mountains, each on the order of 1000 m in elevation: Mount Susitna, Little Mount Susitna, unnamed (south of Wolf Lakes), and Beluga Mountain (Fig. 11a). The BILR is bounded to the northeast by the Susitna basin and the Beluga Mountain fault, to the south by Castle Mountain fault and the Cook Inlet basin, and to the west by a north-south physiographic low that is the drainage for the Talachulitna River, which flows north.

The Beluga region (Fig. 11a) contains a seismic lineament named the Talachulitna seismic zone (TSZ) by Flores and Doser (2005). The TSZ is approximately aligned with the western margin of the BILR, near the Talachulitna River. Flores and Doser (2005) interpreted the TSZ to be dipping steeply to the northeast (their Fig. 4c). The scatter in their results—and ours (Fig. 11a)—prevents us from identifying any alignment with depth.

Earthquake mechanisms are challenging to estimate for the TSZ. Flores and Doser (2005) tabulated one focal mechanism in this zone (AF2; their Table 2), from the AEC focal mechanism catalog, but the current AEC catalog has only five events (Fig. 12b), none of which predate 2005. We present moment tensors for 9 events, all of which are shallower than 12 km (Table S2). The mechanisms have considerable variation, with a predominance of thrust faulting consistent with east-west compression (Fig. 11a).

Regional geophysical data and geological data provide context for the active seismicity. The BILR is mainly composed of Cenozoic and Mesozoic intrusive and volcanic rocks (Ridgway et al., 2012; LePain et al., 2015) that are adjacent to Cenozoic sedimentary basins to the north (Susitna), west (Beluga), and south (Cook Inlet) (Fig. 1b). Hackett (1977) and Saltus et al. (2016) used gravity data and magnetic data to identify the Beluga Mountain fault on the northern front of the BILR as a thrust fault dipping southwest; however recent fault kinematic data do not support a thrust interpretation (Gillis et al., 2015). The Beluga Mountain fault does not appear to be seismically active or connected with the Talachulitna seismic zone.

Examining Fig. 11a, we speculate that the Talachulitna seismic zone represents a north-striking, east-dipping thrust fault system that may represent some weakness within the crustal block north of the Castle Mountain fault and west of Susitna basin. This weakness, aligned with the western margin of the BILR, could accommodate some regional compression and contribute to uplift of the BILR.

5.1.2. Upper Cook Inlet region

Earthquakes in the upper Cook Inlet region occur beneath Cook Inlet basin, a large, long-lived forearc sedimentary basin whose Cenozoic strata have a maximal thickness of 7.6 km and overlie a Mesozoic section approximately 8 km thick (Fisher and Magoon, 1978; Shellenbaum et al., 2010; LePain et al., 2013). The Cook Inlet basin is bounded by the Aleutian Range to west, the Alaska Range and Talkeetna Mountains to the north, and the Kenai and Chugach Mountains to the east (see Fig. 1). On the north, the Castle Mountain Fault separates the Cook Inlet basin from the adjoining Susitna basin. The similarities in structures of Cook Inlet and Susitna basins suggests that their histories are linked (LePain et al., 2013).

The 22 events in our study (Fig. 11b, Table S3) mostly have depths in the 10–20 km range, placing them either within the Mesozoic strata or the crystalline basement. The crust within upper Cook Inlet (north of West Foreland) is more seismically active than the lower Cook Inlet;

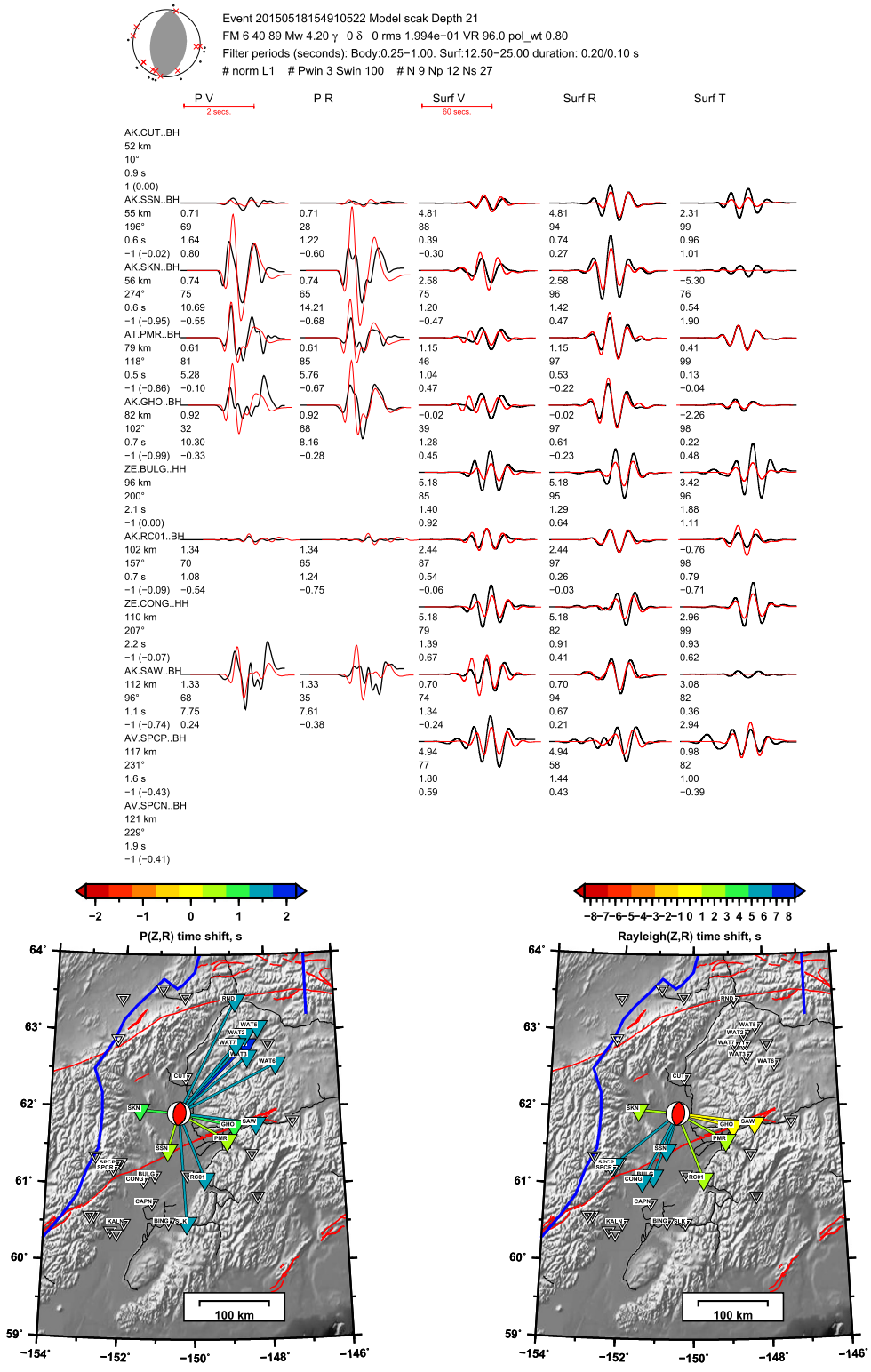

Fig. 9. (top) Waveform fits at subset of stations used for a M_w4.2 crustal earthquake in the Susitna region. See Table S4 for source parameters. Waveform fits for all stations, and for all events, are available (Silwal, 2018). (bottom) Map of time shifts between observed and synthetic waveforms for the P waves (left) and Rayleigh waves (right). Open triangles denote stations with available waveforms that were not used in the inversion. Station names are listed if either the waveform or first-motion polarity was used. Note the large positive time shift for Rayleigh waves traveling to the southwest, through basins. This indicates that along these paths the assumed 1D model is too fast relative to the actual Earth structure. (For interpretation of the references to color in this figure, the reader is referred to the web version of this article.)

this is possibly related to the underlying subduction of the Yakutat microplate (Eberhart-Phillips et al., 2006; Haeussler, 2008).

Folds in Cook Inlet are complex, discontinuous structures with variable shape and vergence that probably developed by right-transpressional deformation on oblique-slip faults extending downward into the Mesozoic strata beneath the Cenozoic basin (Haeussler et al., 2000). A discussion of the complex folding and faulting structures in the basin can be found in Fisher and Magoon (1978) and Haeussler and Saltus (2011).

Our moment tensor inversions for 22 earthquakes reveal thrust fault mechanisms whose strike angles are generally aligned with the Cook Inlet anticlines (Haeussler et al., 2000; Koehler et al., 2012) (Fig. 11b). The simplest explanation is that the anticline structures, identified within active-source seismic data, arise from NW–SE thrust faulting identified from modern earthquakes.

5.1.3. Susitna region

The Susitna region exhibits diffuse seismicity with the larger

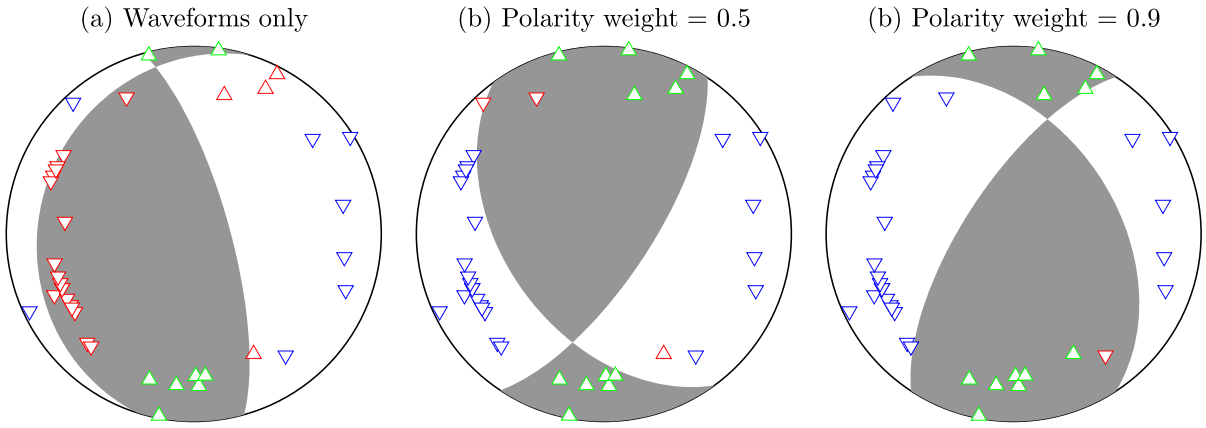

Fig. 10. Impact of using different weights for the polarity misfit, shown for an example earthquake in Cook Inlet (eid 20150727022154395). Each beachball shows the best-fitting moment tensor for a given m in Eq. (3). Triangles denote lower-hemisphere piercing points for each ray path from source to station; these are calculated using an assumed 1D Earth model. Upward triangles denote upward polarity observations; downward triangles denote downward polarity observations. The color indicates agreement or not with predicted polarities: red (up or down) indicates mismatch, while green (up) and blue (down) indicate agreement. See Section 3.3 for details on the misfit function. (a) Waveforms only. Note that a large number of polarity mismatches occur. See Fig. S6 for waveform fits. (b) Waveforms plus polarities with weight factor 0.5. Here, only three polarity measurements are mismatched. See Fig. S7 for waveform fits. (c) Waveforms plus polarities with weight factor 0.9. All observed polarities are fit, except one (in red). See Fig. S8 for waveform fits. (For interpretation of the references to color in this figure legend, the reader is referred to the web version of this article.)

earthquakes (22 in this study) exhibiting thrust fault mechanisms (Fig. 11c, Table S4). These mechanisms, with NW–SE P-axes, are consistent with the convergence direction of N21 W (Bird, 2003) between the Pacific and North America plates. They are also consistent with the interpretation of subsurface contractional structures in the region (Saltus et al., 2016). Further work is needed to relate the stresses within the crust to stresses arising from the subducting slab; such an effort should take into account the microplate setting (Freymueller et al., 2008) and continuum mechanical modeling (e.g., Koons et al., 2010; Jadamec et al., 2013).

The earthquakes in the Susitna region occur within a tectonically complicated region. The region is marked by the Susitna basin (Fig. 3b) (Kirschner, 1988; Wilson et al., 2009), which is bounded by the Alaska Range to the north, the Talkeetna Mountains to the east, the BILR (and Beluga Mountain fault) to the west, and the Castle Mountain fault to the south. The crustal earthquakes are vertically bounded by the overlying Susitna basin and the underlying subducting Pacific plate. The Pacific plate exhibits two transitions in this region: (1) a kink in its geometry (e.g., Fig. 6), from western dipping to more northwestern dipping (Ratchkovski and Hansen, 2002) and (2) an interpreted transition from normal subducting crust in the west to overthickened Pacific/Yakutat crust in the east (Fig. 1a). It is possible that either, or both, of these slab-related features contributes to the concentration of crustal seismicity in the eastern part of the Susitna region.

Comparison between the crustal earthquakes and the basement surface (Fig. S12c) reveals several earthquakes below the deepest part of Susitna basin and within the uppermost 10 km. It is possible that these earthquakes occur on deeper extensions of the structures mapped within the subsurface basin structures (Lewis et al., 2015; Haeussler et al., 2017b). The diffuse seismicity in the eastern portion of the Susitna region underlies the shallowest portion of the basin and are not associated with any previously identified subsurface structures. However, it is worth noting that the lack of faults could be related to the lack of data, as no seismic reflection studies have been done in the eastern part of the Susitna basin (east of the Susitna River), as far as we know.

5.2. Implications of minor earthquakes for active faults

From our perspective, seismic evidence for an active fault includes: (1) alignment of seismicity into a lineament (2) occurrence of moment tensors with one of its two possible fault planes parallel to the lineament, and (3) occurrence of large ($M \geq 6$) earthquakes. This seismic evidence should be assessed alongside geological evidence, whether in the form of slip rates inferred from dated offset units at the surface, from structural offsets inferred from seismic imaging and potential field data, and from paleoseismic evidence of past large earthquakes (Haeussler et al., 2002; Koehler et al., 2012; Saltus et al., 2016; Koehler and Carver, 2018).

Our presentation in Fig. 11 displays these three types of seismic evidence: relocated hypocenters of modern earthquakes, source mechanisms for the largest modern earthquakes, and estimated epicenters of the largest two historical earthquakes, in 1933 and 1943. We also superimpose previously published faults, and here we discuss the possible connections between faults identified from surface and subsurface geological data with seismic activity at depth.

Most of the relocated seismicity does not exhibit seismic lineaments (Section 4). The only lineament we are confident about is the previously identified (Flores and Doser, 2005) Talachulitna seismic zone (Fig. 11a). There is no fault mapped near this lineament (Fig. 11a). It is possible that this seismic zone is an expression of a single fault, but the source mechanisms are variable, and there is no definitive evidence for hosting any moderate or large earthquake. To the northeast, within the Susitna region (Fig. 11c), the seismicity is diffuse but the mechanisms are more consistent, exhibiting thrust faulting. Deformation within the crust appears to be broadly distributed, rather than concentrating on a few discrete faults. The same pattern is true to the south, within the upper Cook Inlet region (Fig. 11c): diffuse seismicity with consistent thrust fault mechanisms. In both the Susitna region and the upper Cook Inlet region, there are subsurface fault and fold structures identified from modeling seismic reflection data and potential field data (gravity and magnetics). If these identified faults penetrate the basement rocks that underlie the sedimentary basin fill (Fig. 3b), then it seems reasonable to ascribe the style of faulting inferred from the earthquake mechanisms to the style of faulting occurring near the surface. Therefore, on the basis of our results from small, recent earthquakes (Fig. 11), we would ascribe thrust faulting to the active folds in Cook Inlet basin (Haeussler et al., 2000) and thrust faulting to the structures in Susitna basin (Lewis et al., 2015; Haeussler et al., 2017b). This is in contrast to the existing catalog of earthquake mechanisms, which favors strike-slip faulting in these regions (Fig. 12b). With all evidence taken together—not just modern earthquakes—it is likely that a range of strike-slip, thrust, and oblique faulting is possible in Cook Inlet and Susitna

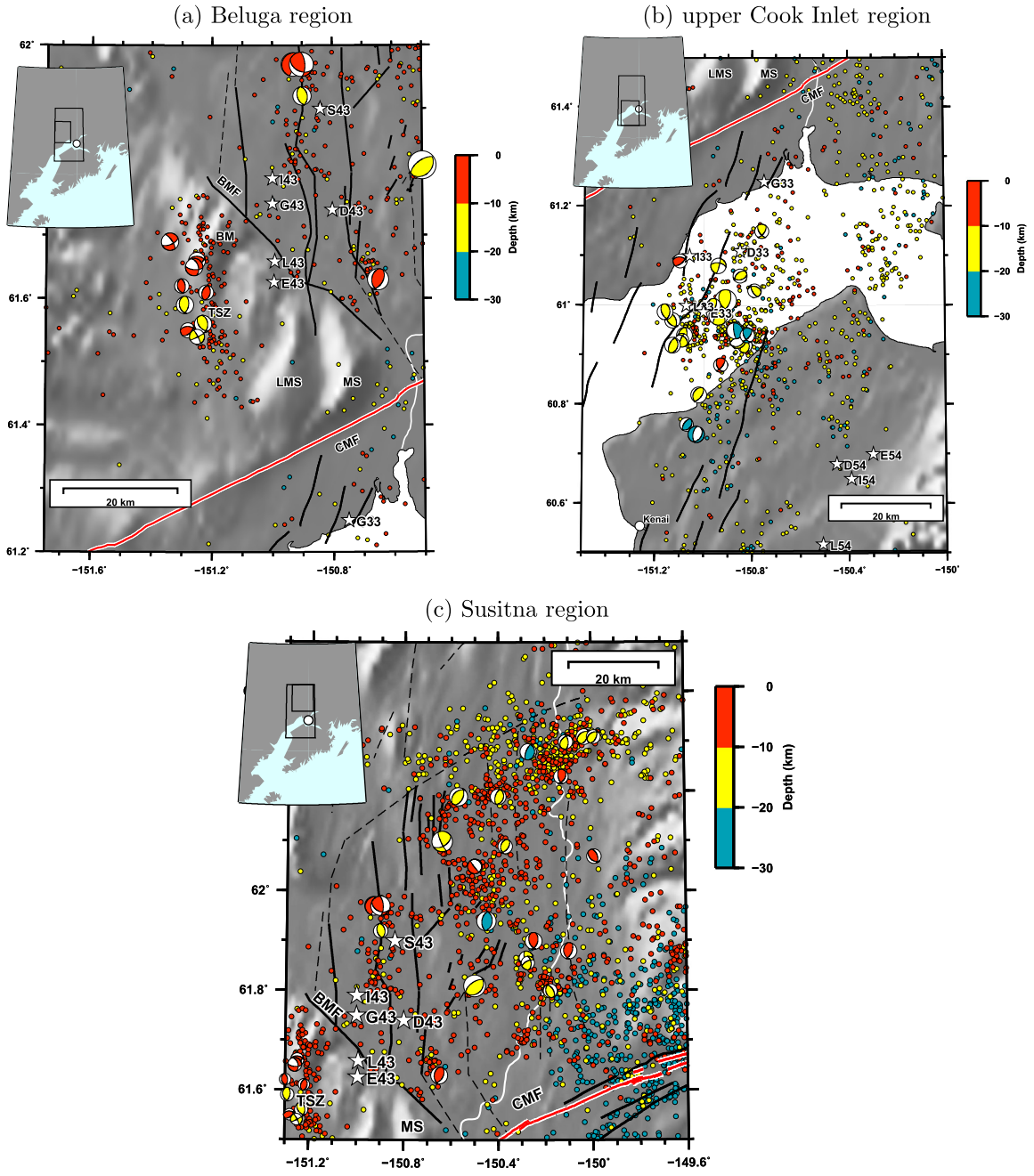

Fig. 11. Our double couple moment tensor solutions for crustal earthquakes (depth ≤ 30 km) between 2007-08-15 and 2017-01-01 in three focus regions (Table 1). The displayed regions are slightly larger than the bounding regions listed in Table 1. The color of each moment tensor (beachball) is related to its depth and its size to its magnitude. Also shown are relocated seismicity (Fig. 13) and previously published epicenters for the 1933, 1943, and 1954 earthquakes, plotted as stars (Table S1:). The maximum likelihood epicenters from this study are labeled as L33, L43, and L54. Text labels: CMF = Castle Mountain fault, BMF = Beluga Mountain fault, BM = Beluga Mountain, LMS = Little Mount Susitna, MS = Mount Susitna, TSZ = Talachulitna seismic zone. Note that the dots here show seismicity, whereas the dots in Fig. 6 show our posterior epicenters for the three historical earthquakes. (a) $M_w \geq 2.5$ in the upper Cook Inlet region. (b) $M_w \geq 2.5$ in the Beluga region. (c) $M_w \geq 3.0$ in the Susitna region. See Fig. S12 for an alternative version of this figure that includes the basement surface. (For interpretation of the references to color in this figure legend, the reader is referred to the web version of this article.)

region. See Fig. 8 of Haeussler et al. (2017a) for a comparison of regional tectonic models.

5.3. Structures responsible for 1933, 1943, and 1954 earthquakes

Large earthquakes rupture along faults with dimensions of tens of kilometers. Previous studies of large sets of earthquakes provides scaling between magnitude and fault dimensions. Assuming a circular fault (radius r, fault dimension $2r$) and a stress drop between 0.2 MPa and 20 MPa (Shearer et al., 2006), the corresponding fault dimension would be

- 15–70 km for the 1933 M_w6.8 earthquake
- 27–125 km for the 1943 M_w7.3 earthquake
- 10–44 km for the 1954 M_w6.4 earthquake

The empirical relationships of Mai and Beroza (2000) are also within these ranges. These dimensions should be kept in mind when

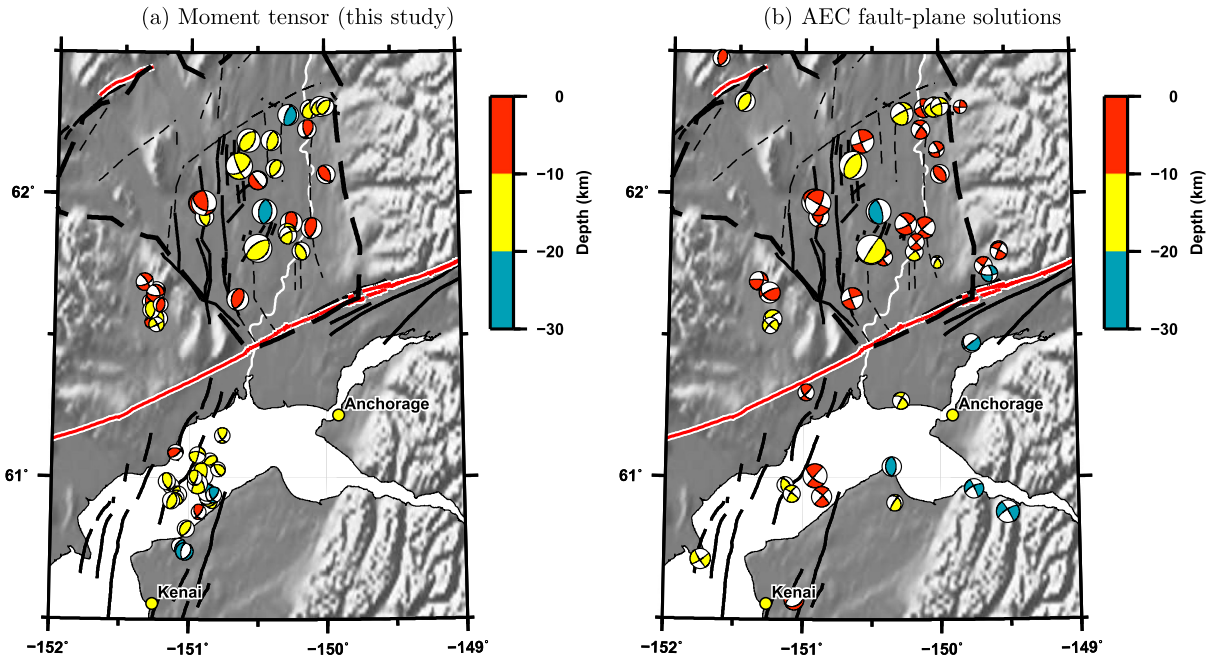

Fig. 12. Comparison between moment tensors in this study and an existing catalog. All earthquakes shown are for depth ≤ 30 km and between 2007-08-15 and 2017-01-01. (a) Moment tensors estimated in this study: 53 total, 26 of which are in (b), 27 which are new. These mechanisms are estimated from waveforms and first-motion polarities. (b) Moment tensors in the Alaska Earthquake Center fault-plane catalog: 46 total, 26 of which are in (a), 20 of which we do not examine. These mechanisms are estimated from first-motion polarities.

examining Figs. 6 and 11.

Our probabilistic hypocentral estimations for the 1933, 1943, and 1954 earthquakes (Fig. 6, Section 2.1) provide a starting point for interpreting the structures responsible (and not responsible) for these earthquakes. The 1933 earthquake (Fig. 6) occurred within the region of the concentration of modern earthquakes in the upper Cook Inlet region (Fig. 11b). It seems possible that one of the northeast-striking thrust faults could have hosted the 1933 earthquake (Haeussler et al., 2000). The 1943 earthquake (Fig. 6) maximum likelihood epicenter is on the Beluga Mountain fault (L43 label in Fig. 11c), yet the uncertainty region for the epicenter (Fig. 6) also includes some of the north-striking faults in Susitna basin, as well as the Talachulitna seismic zone (Fig. 11a). Therefore, all of these faults are candidates for the 1943 earthquake.

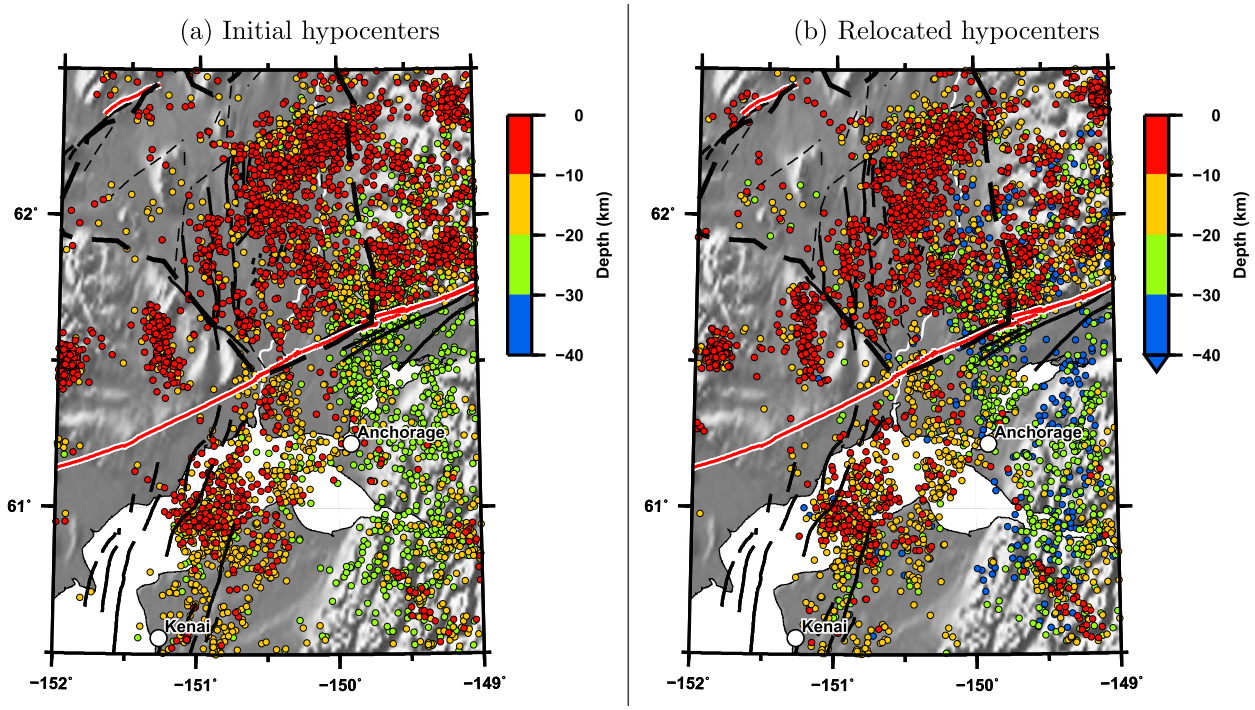

Fig. 13. Relocation of hypocenters using a double-difference approach. The crustal earthquakes considered have depth ≤ 30 km, M_w ≥ 1.5, and occurred between 1990-01-01 and 2017-01-01. See Section 4 and Fig. S14 for details.

Reliable source mechanisms for historical earthquakes would provide valuable constraints on the (unknown) host faults. Here we summarize results, and challenges, from Doser and Brown (2001), who estimated source mechanisms for the 1933, 1943, and 1954 earthquakes, among others. They used limited teleseismic data to estimate the source mechanisms: P, PP, and S waveforms for 13 global stations, as well as first-motion polarities, where available. (By comparison, there are > 100 global stations providing arrival times used in Figs. 6 and 5.) They present waveform comparisons for all events in their Fig. A2, offering the reader the chance to assess the reliability of the results. The numbers of stations and waveforms used for each event were as follows: 3 stations (8 waveforms) for 1933, 5 stations (9 waveforms) for 1943, 6 stations (11 waveforms) plus first-motion polarities for 1954. Surface waves were not used, though they provide stable constraints for global moment tensor inversions (Duputel et al., 2012; Dziewonski et al., 1981), mainly owing to the insensitivity of their long periods to 3D structural heterogeneities in Earth.

The picture of faulting from the 1933 and 1943 mechanisms (Doser and Brown, 2001) is one of strike-slip faulting (Fig. 6), either right-lateral on a northeast-striking fault or left-lateral on a northwest-striking fault. Based on the points above, and from our own experience examining moment tensor uncertainties with modern regional earthquakes (Silwal and Tape, 2016), we would advise caution in basing any interpretation on the historical mechanisms. For example, rotation of these beachballs by 90° about their P-axes would lead to a north-striking thrust fault that would satisfy some of the historical seismic waveforms and first-motion polarities. Our epicenter locations for 1933 and 1943 earthquakes support the findings of Doser and Brown (2001) and exclude the Castle Mountain fault as a source for the two earthquakes.

The 1954 earthquake likely occurred within the subducting Pacific plate, rather than on the subduction interface or within the lower overriding crust. The depth distribution of modern seismicity in this region is nearly continuous (Fig. 7c, Fig. 1b), making it challenging to discriminate among the three possibilities. This event has the benefit of better data than the older events, and therefore the mechanism should be more reliable. Two source mechanisms from previous studies are shown in Fig. 6 and reveal strike-slip faulting, not low-angle thrust faulting that would be expected for the subduction interface.

6. Summary

We present a seismological study of the tectonically complex region of Cook Inlet and Susitna, west of Anchorage, Alaska (Fig. 1), with emphasis on crustal earthquakes. Using arrival time data, we estimate hypocenters of all 11 historical earthquakes $M_w \geq 5.8$ that have occurred in the Cook Inlet and Susitna region. Using waveforms from modern earthquakes, we estimate source mechanisms for 53 crustal earthquakes (M_w 2.5 to 4.8). Using arrival time data, we relocate a catalog of 5726 earthquakes ($M_l \geq 1.5$). We examine these seismological results in the context of regional tectonics, regional structures (basins, faults, folds), and previously published source mechanisms of older (and larger) earthquakes.

Here, we summarize our main findings:

1. Within the Cook Inlet and Susitna region, we can generalize the earthquake patterns into two time periods (Fig. 4). In the last several decades there have been small-magnitude thrust events in the crust and larger events in the slab. Prior to 1950 or so there have been large-magnitude crustal earthquakes that were possibly strike-slip. The existence of two crustal earthquakes (1933 M_w6.8 and 1943 M_w7.3) motivates our examination of modern crustal earthquakes and geological structures. Within our three focus regions (Fig. 8, the crust has not produced notable earthquakes in the recent decades of high-quality seismic data: there are zero crustal earthquakes in the GCMT catalog (Dziewonski et al., 1981: 1976–2018). (The 1984 and 1996 earthquakes occurred to the east: Fig. 6.)
2. Our source mechanisms favor an interpretation of thrust faulting (Fig. 12a) over strike-slip faulting (Fig. 12b). Uncertainties in the source mechanisms are considerable, owing to the small magnitudes (which limits the inclusion of surface waves) and the extreme crustal heterogeneity (notably basins: Fig. 3b), which was not accounted for in modeling synthetic seismograms.
3. Seismicity in the Susitna region (Fig. 11c, Fig. 13) is diffuse (Ratchkovsky et al., 1998). As discussed in Section 5.1, the deforming crust in this region may be influenced by forces arising from subduction, either from the underlying slab or from tractions of the flowing mantle (Haeussler and Saltus, 2011; Ridgway et al., 2012).
4. The 1933 M_w6.8 earthquake occurred beneath Cook Inlet basin, in a region exhibiting northeast-striking thrust fault source mechanisms (Fig. 11b) that are aligned with the axes of active fold anticlines (Haeussler et al., 2000). It is possible that the 1933 earthquake ruptured as a thrust fault, though the previously published source mechanism (using three stations) is a strike-slip mechanism. Haeussler et al. (2000) suggested that a fault-cored anticline within Cook Inlet could have hosted the 1933 earthquake, and Doser and Brown (2001) concurred, though neither study ruled out the Castle Mountain fault as a source.
5. The 1943 M_w7.3 Susitna earthquake is the fourth largest earthquake ever to occur in mainland Alaska, following 1964 M_w9.2 megathrust, 2002 M_w7.9 Denali fault, and 1979 M_w7.4 Wrangell–St. Elias. Its hypocenter was beneath the Susitna basin, possibly on a structure associated with the Beluga Mountain fault or the Talachulitna seismic zone (Fig. 11a). A previous study used waveforms from five stations (Doser and Brown, 2001) to estimate a strike-slip source mechanism for the earthquake (Fig. 6). Moment tensors of crustal events closest to the 1943 epicenter exhibit thrust mechanisms, consistent with inferred subsurface structures (Lewis et al., 2015; Saltus et al., 2016). Either a strike-slip or a thrust fault seems most likely for the 1943 earthquake.
6. The 1954 M_w6.4 earthquake beneath the Kenai Peninsula was likely an intraslab earthquake. It produced the strongest shaking (MMI 8) ever documented on the western Kenai Peninsula (Appendix A). The subducting Pacific plate has produced much larger intraslab earthquakes, such as the deeper and more distant M_w7.1 earthquake on 2016-01-24. For considering ground motion calculations from potential earthquakes in the region ("scenario earthquakes"), it is worth considering a M_w7.0 earthquake in the 1954 hypocentral region.

Acknowledgments

This project was supported by the Earthquakes Hazards Program of the United States Geological Survey, AwardG15AP00052. Our manuscript benefitted from reviews by Diane Doser and Richard Stanley and feedback from Rich Koehler and Peter Haeussler. Digital files for faults in the Susitna basin region were provided by Anjana Shah, Richard Stanley, and Peter Haeussler. Thanks to Lea Gardine for converting digital fault files from GIS format to text format. Digital files for the basement surface of Susitna and Peters Hill basins (Fig. 3b) were provided by Jeff Phillips at USGS. We thank Domenico Di Giacomo of the International Seismological Centre for providing arrival time data for six of the historical earthquakes presented here and in Lomax et al. (2018): 1929-07-03, 1933-06-12, 1933-06-13, 1933-06-19, 1936-10-23, and 1937-10-24. We thank Celso Alvizuri for code developments for data processing and moment tensor inversions.

Appendix A. Summary of felt reports for 1933, 1943, and 1954 earthquakes

Here, we summarize the entries for the 1933, 1943, and 1954 earthquakes within the annual earthquake volumes of the U.S. Coast

and Geodetic Survey (Neumann, 1935; Bodle, 1945; Murphy and Cloud, 1956). See felt report locations on maps in Fig. S15.

A.1. 1933-04-27 M_w6.8

The complete entry in Neumann (1935):

April 26: 16:36*. Instrumental epicenter 62° north, 151° west. Anchorage, VI. Telegraph lines were down for a distance of 50 miles from Anchorage. The shock lasted about 3 minutes. Plate glass windows in several stores were broken and stocks of good tumbled from their shelves. This earthquake was considered by residents as the worst in 30 years. The quake was felt strongly on Kodiak Island and along the Aleutian Islands. It was felt strongly at Curry, McGrath, Seward, and Wasilla; Dillingham (Kanakanak), IV; reported light at Healy. The shock was felt at College, Fairbanks, Susitna, Valdez, and Whale Island.Because of the difficulty in correlating the times of occurrence of the following aftershocks it has been considered best to list them all as individual shocks, even though it is evident that this is not always true.*April 26:* Homer; earthquake and following tremors.*April 26:* Kasilof;*April 26:* Big Susitna River District, VII.*April 26:* Old Tyonek, VII. Houses shaken off foundations.

A.2. 1943-11-03 M_w7.3

The complete entry in Bodle (1945):

November 3: 04:32.3.* Anchorage. Sharp shock with abrupt heaving motion made doors swing and windows rattle. Generally felt. A light after-shock occurred at 05:40. Several slight tremors were felt at intervals until about 07:30. Pen on recording rain gage made mark about $\frac{3}{4}$ inch wide at time of main shock. Similar marks were recorded on the barograph traces. Epicenter probably near 62° north, 151° west. Felt at McGrath 04:33. Slight shock reported by Weather Bureau Observer as continuing for about fifteen seconds. “Wall clocks in the Civil Aeronautics Administration and Weather Bureau Offices were stopped. The baragraph trace showed no indication of the quake …. ”Felt at Bethel 04:37. Tremors lasting 20 seconds were felt by several. Faint rumbling underground and moderately loud cracking of ice was heard. Building swayed. “The noise moved down the river quickly and then seemed to pass under the station making the earth tremble comparable to a locomotive passing. The ice in the river made a cracking noise for about an hour after the tremors, which lasted about 20 seconds.”

Following Bodle (1945), Brockman et al. (1988) lists only three felt reports (Anchorage, McGrath, and Bethel), but we found 10 additional felt reports within the monthly weather records. Furthermore, p. 4 of the 1943-11-03 Fairbanks Daily News-Miner had an articles headlined “Big Quake Felt Here This Morn”. We speculate that the shortage of reports in Bodle (1945) was due to the national focus on WWII, which may have limited other duties such as earthquake compilations.

A.3. 1954-10-03 M_w6.4

The complete entry in Murphy and Cloud (1956):

October 3: 01:18:46*. Epicenter $60\frac{1}{2}^{\circ}$ north, 151° west, Kenai Peninsula, W. VIII. A sharp earthquake rocked a 1000 square mile area of the lower Alaska mainland. Concrete walls cracked; plaster showered down; plate glass windows shattered; merchandise toppled from shelves at Anchorage, Homer, Kenai, Seward, Sterling, and Valdez. Minor landslides spilled down on the Seward-Anchorage highway. More than 140 feet of railroad tracks were knocked out of commission just north of Potter. Residents on top floors in Anchorage's two 14-story “skyscrapers” fled into the streets when the violent rocking broke water connections. At the Denali Theater, where a midnight show was in progress, some 850 patrons rushed toward the exists [sic], climbing over seats in a frenzy to escape. Three persons were reported injured slightly in the rush. Motorists driving cars at the time of the quake said it felt “like moving along on a flat tire.” It was also felt at Cordova, Eklutna, Fairbanks, Kasilof, Kodiak, Latouche, Mantanuska [sic] Agricultural Experiment Station, Moose Pass (severe enough to shake things from the shelves), Palmer, Puntilla, and Yakutat. Five aftershocks of a few seconds duration followed the main quake at 02:43, 05:21, 05:34, 06:18, and 07:26.

The MMI VIII shaking intensity for the 1954 M_w6.4 earthquake was the largest ever reported on the western Kenai Peninsula (Homer, Kenai, Sterling) — even exceeding the MMI VII of the 1964 M_w9.2 earthquake (Brockman et al., 1988).

Appendix B. Supplementary data

Supplementary data to this article can be found online at https://doi.org/10.1016/j.tecto.2018.08.013.

References

Abe, K., 1981. Magnitudes of large shallow earthquakes from 1904 to 1980. Phys. Earth Planet Inter. 27, 72–92.

Abers, G., Christensen, D., 2006. Seismic and Geodetic Imaging of Subducting Terranes under North America. International Federation of Digital Seismograph Networks. Other/Seismic Networkhttps://doi.org/10.7914/SN/YV_2006.

Alvizuri, C., Silwal, V., Krischer, L., Tape, C., 2018. Estimation of full moment tensors, including uncertainties, for nuclear explosions, volcanic events, and earthquakes. J. Geophys. Res. Solid Earth 123, 5099-Ű5119. https://doi.org/10.1029/2017JB015325.

Alvizuri, C., Tape, C., 2018. Full moment tensor analysis of nuclear explosions in North Korea. Seismol. Res. Lett (in press).

Alvizuri, C., Tape, C., 2016. Full moment tensors for small events (M_w < 3) at Uturuncu Volcano, Bolivia. Geophys. J. Int. 206, 1761–1783. https://doi.org/10.1093/gji/ggw247.

Amante, C., Eakins, B.W., 2009. ETOPO1 1 Arc-minute Global Relief Model: Procedures, Data Sources and Analysis. In: NOAA Technical Memorandum NESDIS NGDC-24, pp. 19.

Bird, P., 2003. An updated digital model of plate boundaries. Geochem. Geophy. Geosyst. 4, 1–52. https://doi.org/10.1029/2001GC000252.

Bodle, R.R., 1945. United States Earthquakes 1943. U.S. Department of Commerce.

Bondár, I., Storchak, D., 2011. Improved location procedures at the international seismological centre. Geophys. J. Int. 186, 1220–1244. https://doi.org/10.1111/j.1365-246X.2011.05107.x.

Brockman, S.R., Espinosa, A.F., Michael, J.A., 1988. Catalog of intensities and magnitudes for earthquakes in Alaska and the Aleutian Islands—1786-1981. U.S. Geol. Surv. Bull. 1840.

Bruhn, R.L., Haeussler, P.J., 2006. Deformation driven by subduction and microplate collision: geodynamics of Cook Inlet basin, Alaska. Geol. Soc. Am. Bull. 118 (3/4), 289–303.

Capps, S.R., 1913. The Yentna district Alaska. U.S. Geol. Surv. Bull. 534 USGS, Washington D.C.. https://pubs.usgs.gov/bul/0534/report.pdf.

International Seismological Centre, 2015. On-line Bulletin. http://www.isc.ac.uk Internatl. Seis. Cent., Thatcham, United Kingdom (accessed 2017-05-03) (2015).

International Seismological Centre, 2018. ISC-GEM Global Instrumental Earthquake Catalogue. Version 5.0, released on 2018-02-27.

Chiang, A., Dreger, D.S., Ford, S.R., Walter, W.R., 2014. Source characterization of underground explosions from combined regional moment tensor and first-motion analysis. Bull. Seismol. Soc. Am. 104 (4), 1587–1600. https://doi.org/10.1785/0120130228.

Christeson, G.L., Gulick, S.P.S., van Avendonk, H.J.A., Worthington, L.L., Reece, R.S., Pavlis, T.L., 2010. The Yakutat terrane: dramatic change in crustal thickness across the Transition fault, Alaska. Geology 38 (10), 895–898.

Crotwell, H.P., Owens, T.J., Ritsema, J., 1999. The TauP toolkit: flexible seismic travel-time and ray-path utilities. Seismol. Res. Lett. 70 (2), 154–160.

Davies, J., Sykes, L., Jacob, K., 1981. Shumagin seismic gap, Alaska Peninsula: history of great earthquakes, tectonic setting, and evidence for high seismic potential. J. Geophys. Res. 86 (B5), 3821–3855.

Doser, D.I., 2005. Historical seismicity (1918–1964) of the Kodiak Island region. Bull. Seismol. Soc. Am. 95 (3), 878–895. https://doi.org/10.1785/0120040175.

Doser, D.I., 2006. Relocations of earthquakes (1899–1917) in south-central Alaska. Pure App. Geophys. 163, 1461–1476. https://doi.org/10.1007/s00024-006-0085-3.

Doser, D.I., Brown, W.A., 2001. A study of historic earthquakes of the Prince William Sound, Alaska, Region. Bull. Seismol. Soc. Am. 91 (4), 842–857.

Douglas, A., 1967. Joint epicentre determination. Nature 215, 47–48.

Duputel, Z., Rivera, L., Kanamori, H., Hayes, G., 2012. W phase source inversion for

moderate to large earthquakes. Geophys. J. Int. 189, 1125–1147.
Dziewonski, A., Chou, T.A., Woodhouse, J.H., 1981. Determination of earthquake source parameters from waveform data for studies of global and regional seismicity. J. Geophys. Res. 86 (B4), 2825–2852. https://doi.org/10.1029/JB086iB04p02825.
Eberhart-Phillips, D., Christensen, D.H., Brocher, T.M., Hansen, R., Ruppert, N.A., Haeussler, P.J., Abers, G.A., 2006. Imaging the transition from aleutian subduction to Yakutat collision in central Alaska, with local earthquakes and active source data. J. Geophys. Res. 111. https://doi.org/10.1029/2005JB004240.
Ekström, G., Nettles, M., Dziewoński, A.M., 2012. The global GCMT project 2004–2010: centroid-moment tensors for 13,017 earthquakes. Phys. Earth Planet. Inter. 200-201, 1–9. https://doi.org/10.1016/j.pepi.2012.04.002.
Engdahl, E.R., Villasenor, A., 2002. Global seismicity: 1900–1999. In: Lee, W.H.K., Kanamori, H., Jennings, P.C., Kisslinger, C. (Eds.), International Handbook of Earthquake and Engineering Seismology. International Geophysics Series, vol. 81A. Academic Press, London, pp. 665–690.
Engdahl, E.R., van der Hilst, R., Buland, R., 1998. Global teleseismic earthquake relocation with improved travel times and procedures for depth determination. Bull. Seismol. Soc. Am. 88 (3), 722–743.
Fisher, M.A., Magoon, L.B., 1978. Geologic framework of lower Cook Inlet. Am. Assoc. Petroleum Geol. Bull. 62 (3), 373–402.
Flores, C., Doser, D.I., 2005. Shallow seismicity of the Anchorage, Alaska, region (1964–1999). Bull. Seismol. Soc. Am. 95 (5), 1865–1879. https://doi.org/10.1785/0120040121.
Ford, S.R., Walter, W.R., Dreger, D.S., 2012. Event discrimination using regional moment tensors with teleseismic-*p* constraints. Bull. Seismol. Soc. Am. 102 (2), 867–872. https://doi.org/10.1785/0120110227.
Freymueller, J.T., Woodard, H., Cohen, S.C., Cross, R., Elliott, J., Larsen, C.F., Hreinsdóttir, S., Zweck, C., 2008. Active deformation processes in Alaska, based on 15 years of GPS measurements. In: Freymueller, J.T., Haeussler, P.J., Wesson, R., Ekström, G. (Eds.), Active Tectonics and Seismic Potential of Alaska. Geophysical Monograph, vol. 179. Am. Geophys. Un., Washington, D.C., pp. 1–42.
Fu, Y., Freymueller, J.T., 2013. Repeated large Slow Slip Events at the south central Alaska subduction zone. Earth Planet. Sci. Lett. 375, 303–311.
Giacomo, D.D., Bondár, I., Storchak, D.A., Engdahl, E.R., Bormann, P., Harris, J., 2015. ISC-GEM: Global instrumental earthquake catalogue (1900–2009), III. Re-computed MS and mb, proxy MW, final magnitude composition and completeness assessment. Phys. Earth Planet. In. 239, 33–47. https://doi.org/10.1016/j.pepi.2014.06.005.
Gillis, R.J., Herriott, T.M., Tsigonis, R.M., 2015. Preliminary results of reconnaissance structural studies of the western Susitna basin, south-central Alaska. In: Preliminary Interpretive Report 2015-3-5, https://doi.org/10.14509/29469.
Grantz, A., 1966. Strike-slip faults in Alaska. In: U.S. Geol. Survey Open-File Report 66-53, Washington, D.C..
Guilhem, A., Hutchings, L., Dreger, D.S., Johnson, L.R., 2014. Moment tensor inversions of $M \sim 3$ earthquakes in the geysers geothermal fields, California. J. Geophys. Res. Solid Earth 119 (3), 2121–2137. https://doi.org/10.1002/2013JB010271.
Gutenberg, B., Richter, C.F., 1954. Seismicity of the Earth and Associated Phenomena, 2nd edition. Princeton U. Press, Princeton, New Jersey, USA.
Hackett, S.W., 1977. Gravity Survey of Beluga Basin and Adjacent Area, Cook Inlet Region, Southcentral Alaska. https://doi.org/10.14509/377.
Haeussler, P.J., 2008. An overview of the neotectonics of interior Alaska Far-field deformation from the Yakutat microplate collision. In: Freymueller, J.T., Haeussler, P.J., Wesson, R., Ekström, G. (Eds.), Active Tectonics and Seismic Potential of Alaska. Geophysical Monograph, vol. 179. Am. Geophys. Un., Washington, D.C., pp. 83–108.
Haeussler, P.J., Best, T.C., Waythomas, C.F., 2002. Paleoseismology at high latitudes: seismic disturbance of upper Quaternary deposits along the Castle Mountain fault near Houston, Alaska. Geol. Soc. Am. 114 (10), 1296–1310.
Haeussler, P.J., Bruhn, R.L., Pratt, T.L., 2000. Potential seismic hazards and tectonics of the upper Cook Inlet basin, Alaska, based on analysis of Pliocene and younger deformation. Geol. Soc. Am. Bull. 112 (9), 1414–1429.
Haeussler, P.J., Matmon, A., Schwartz, D.P., Seitz, G.G., 2017a. Neotectonics of interior Alaska and the late Quaternary slip rate along the Denali fault system. Geosphere 13 (5), 1445–1463. https://doi.org/10.1130/GES01447.1.
Haeussler, P.J., Saltus, R.W., 2004. 26 km of offset on the Lake Clark fault since late Eocene time. In: Haeussler, P.J., Galloway, J.P. (Eds.), U.S. Geological Survey in Alaska, 2004. U.S. Geol. Survey, Washington, D.C., pp. 1–4 Professional Paper 1709-A.
Haeussler, P.J., Saltus, R.W., 2011. Location and extent of Tertiary structures in Cook Inlet basin, Alaska, and mantle dynamics that focus deformation and subsidence. In: Dumoulin, J.A., Galloway, J.P. (Eds.), Studies by the U.S. Geological Survey in Alaska, 2008-2009. U.S. Geol. Survey, Washington, D.C., pp. 1–26 Professional Paper 1776-D.
Haeussler, P.J., Saltus, R.W., Stanley, R.G., Ruppert, N., Lewis, K., Karl, S.M., Bender, A., 2017b. The Peters Hills basin, a Neogene wedge-top basin on the broad pass thrust fault, South-Central Alaska. Geosphere 13 (5), 1464–1488. https://doi.org/10.1130/GES01487.1.
Hauksson, E., Shearer, P., 2005. Southern California hypocenter relocation with waveform cross-correlation, part 1: results using the double-difference method. Bull. Seismol. Soc. Am. 95 (3), 896–903.
Hayes, G.P., Wald, D.J., Johnson, R.L., 2012. Slab1.0: A three-dimensional model of global subduction zone geometries. J. Geophys. Res. 117. https://doi.org/10.1029/2011JB008524.
Ichinose, G., Somerville, P., Thio, H.K., Graves, R., O'Connell, D., 2007. Rupture process of the 1964 Prince William Sound, Alaska, earthquake from the combined inversion of seismic, tsunami, and geodetic data. J. Geophys. Res. 112, 2007. https://doi.org/10.1029/2006JB004728.
Jadamec, M.A., Billen, M.I., 2010. Reconciling surface plate motions with rapid three-dimensional mantle flow around a slab edge. Nature 465, 338-Ű342. https://doi.org/10.1038/nature09053.
Jadamec, M.A., Billen, M.I., Roeske, S.M., 2013. Three-dimensional numerical models of flat slab subduction and the Denali fault driving deformation in South-Central Alaska. Earth Planet. Sci. Lett. 376, 29–42.
Meyer Jr, J.G., 2005. Principal facts for gravity data collected in the northern Susitna basin area, Southcentral Alaska. In: Alaska Div. Geol. Geophys. Surv. Preliminary Interpretive Report 2005-5.
Kennett, B.L.N., Engdahl, E.R., Buland, R., 1995. Constraints on seismic velocities in the Earth from traveltimes. Geophys. J. Int. 122, 108–124.
Kirschner, C.E., 1988. Map showing sedimentary basins of onshore and continental shelf areas, Alaska. In: U.S. Geol. Survey Miscellaneous Investigation Series I-1873.
Koehler, R.D., Carver, G.A., 2018. Active faults and seismic hazards in Alaska. Alaska Div. Geol. Geophys. Surv., Miscellaneous Publication 160. https://doi.org/10.14509/29705.
Koehler, R.D., Farrell, R.E., Burns, P.A.C., Combellick, R.A., 2012. Quaternary Faults and Folds in Alaska: A Digital Database. 141. Alaska Div. Geol. Geophys. Surv. Miscellaneous Publication, pp. 31. https://doi.org/10.14509/23944. 1 sheet, scale 1:3,700,000.
Koehler, R.D., Reger, R.D., Spangler, E.R., Gould, A.I., 2015. Investigation of potentially active tectonic faults along the route of the proposed Alaska stand alone pipeline, Livengood to Cook Inlet, Alaska. In: Alaska Div. Geol. Geophys. Surv., Report of Investigation 2015-4, pp. 71. https://doi.org/10.14509/29409.
Koons, P.O., Hooks, B.P., Pavlis, T., Upton, P., Barker, A.D., 2010. Three dimensional mechanics of Yakutat convergence in the southern Alaskan plate corner. Tectonics 29. https://doi.org/10.1029/2009TC002463.
Lahr, J.C., Page, P.A., Stephens, C.D., Fogleman, K.A., 1986. Sutton, Alaska, earthquake of 1984: evidence for activity on the Talkeetna segment of the Castle Mountain fault system. Bull. Seismol. Soc. Am. 76 (4), 967–983.
LePain, D.L., Stanley, R.G., Harun, N.T., Helmold, K.P., Tsigonis, R.M., 2015. Reconnaissance stratigraphic studies in the Susitna basin, Alaska, during the 2014 field season. In: Preliminary Interpretive Report 2015-3-2, https://doi.org/10.14509/29466.
LePain, D.L., Stanley, R.G., Helmold, K.P., Shellenbaum, D.P., 2013. Geologic Framework and Petroleum Systems of Cook Inlet Basin, South-central Alaska. vol. 104 American Association of Petroleum Geologistshttps://doi.org/10.1306/13491874M1043621.
Lewis, K.A., Potter, C.J., Shah, A.K., Stanley, R.G., Haeussler, P.J., Saltus, R.W., 2015. Preliminary interpretation of industry two-dimensional seismic data from Susitna basin, South-central Alaska. U.S. Geol. Survey open-file report 2015–1138. https://doi.org/10.3133/ofr20151138.
Li, J., Abers, G.A., Kim, Y., Christensen, D., 2013. Alaska megathrust 1: seismicity 43 years after the great 1964 Alaska megathrust earthquake. J. Geophys. Res. 118, 4861–4871. https://doi.org/10.1002/jgrb.50358.
Li, S., Freymueller, J., McCaffrey, R., 2016. Slow slip events and time-dependent variations in locking beneath lower Cook Inlet of the Alaska-Aleutian subduction zone. J. Geophys. Res. Solid Earth 121, 1060–1079. https://doi.org/10.1002/2015JB012491.
Lomax, A., Silwal, V., Tape, C., 2018. Hypocenter Estimation for 14 earthquakes in South-central Alaska (1929-1975). Scholarworks@UA at http://hdl.handle.net/11122/8380: descriptor file and zipped set of text files for each earthquake.
Lomax, A., Virieux, J., Volant, P., Berge, C., 2000. Probabilistic earthquake location in 3D and layered models introduction of a Metropolis-Gibbs method and comparison with linear locations. In: Thurber, C.H., Rabinowitz, N. (Eds.), Advances in Seismic Event Location. Kluwer, Amsterdam, pp. 101–134.
Magoon, L.B., Adkison, W.L., Egbert, R.M., 1976. Map showing geology, wildcat wells, tertiary plant fossil localities, K-Ar age dates, and petroleum operations. In: Cook Inlet Area, Alaska, U.S. Geol. Survey Miscellaneous Investigation Series I-1019.
Mai, P.M., Beroza, G.C., 2000. Source scaling properties from finite-fault-rupture models. Bull. Seismol. Soc. Am. 90 (3), 604–615.
Murphy, L.M., Cloud, W.K., 1956. United States Earthquakes 1954. U.S. Department of Commerce.
Mustać, M., Tkalčić, H., 2016. Point source moment tensor inversion through a Bayesian hierarchical model. Geophys. J. Int. 204, 311–323. https://doi.org/10.1093/gji/ggv458.
Mustać, M., Tkalčić, H., 2017. On the use of data noise as a site-specific weight parameter in a hierarchical Bayesian moment tensor inversion: the case study of the geysers and long valley caldera earthquakes. Bull. Seismol. Soc. Am. 107 (4), 1914–1922. https://doi.org/10.1785/0120160379.
Neumann, F., 1935. United States Earthquakes 1933. U.S. Department of Commerce.
Ohta, Y., Freymueller, J.T., Hreinsdóttir, S., Suito, H., 2006. A large slow slip event and the depth of the seismogenic zone in the south central Alaska subduction zone. Earth Planet. Sci. Lett. 247, 108–116.
Page, R.A., Biswas, N.N., Lahr, J.C., Pulpan, H., 1991. Seismicity of continental Alaska. In: Slemmons, D.B., Engdahl, E.R., Zoback, M.D., Blackwell, D.D. (Eds.), Neotectonics of North America. The Geology of North America Geol. Soc. Am., Boulder, Colo., USA Ch. 4, pp. 47-68, Decade Map Volume 1.
Plafker, G., Gilpin, L.M., Lahr, J.C., 1994. Neotectonic map of Alaska. In: Plafker, G., Berg, H.C. (Eds.), Geology of Alaska. Geology of North America, vol. G-1 Geol. Soc. Am., Boulder, Colo., USA Plate 12.
Plafker, G., Hudson, T.L., Bruns, T., Rubin, M., 1978. Late Quaternary offsets along the Fairweather fault and crustal plate interactions in Southern Alaska. Can J. Earth Sci. 15 (5), 805–816.
Ratchkovski, N.A., Hansen, R.A., 2002. New evidence for segmentation of the Alaska subduction zone. Bull. Seismol. Soc. Am. 92 (5), 1754–1765.
Ratchkovsky, N.A., Pujol, J., Biswas, N.N., 1998. Relocation of shallow earthquakes in southern Alaska using Joint Hypocenter Determination method. J. Seis. 2, 87–102.
Reasenberg, P., Oppenheimer, D., 1985. FPFIT, FPPLOT and FPPAGE: Fortran computer

programs for calculating and displaying earthquake fault-plane solutions. In: Open-File Report 85-739.
Ridgway, K.D., Trop, J.M., Finzel, E.S., 2012. Modification of continental forearc basins by flat-slab subduction processes: a case study from Southern Alaska. In: Busby, C., Perez, A.A. (Eds.), Tectonics of Sedimentary Basins: Recent Advances. Wiley-Blackwel, pp. 327–346. https://doi.org/10.1002/9781444347166.ch16.
Rondenay, S., Montési, L.G.J., Abers, G.A., 2010. New geophysical insight into the origin of the Denali volcanic gap. Geophys. J. Int. 182, 613–630.
Saltus, R.W., Stanley, R.G., Haeussler, P.J., Jones, J.V. III, Potter, C.J., Lewis, K.A., 2016. Late Oligocene to present contractional structure in and around the Susitna basin, Alaska—geophysical evidence and geological implications. Geosphere 12 (5), 1–13. https://doi.org/10.1130/GES01279.1.
Shah, A.K., Stanley, R.G., Lewis, K., Haeussler, P.J., Potter, C.J., Saltus, R.W., Phillips, J.D., 2015. Aeromagnetic survey data used to map features of the Cook Inlet and Susitna basins, Alaska. In: Abstract presented at 2015 AGU-SEG Workshop, Denver, Colo., 25-27 Aug.
Shearer, P., Hauksson, E., Lin, G., 2005. Southern California hypocenter relocation with waveform cross-correlation, part 2: results using source-specific station terms and cluster analysis. Bull. Seismol. Soc. Am. 95 (3), 904–915. https://doi.org/10.1785/0120040168.
Shearer, P.M., Prieto, G.A., Hauksson, E., 2006. Comprehensive analysis of earthquake source spectra in southern California. J. Geophys. Res. 111. https://doi.org/10.1029/2005JB003979.
Shellenbaum, D.P., Gregersen, L.S., Delaney, P.R., 2010. Top mesozoic unconformity depth map of the Cook Inlet basin, Alaska. In: Alaska Div. Geol. Geophys. Surv. Report of Investigation 2010-2, https://doi.org/10.14509/21961.. 1 sheet, scale 1:500,000, available at http://www.dggs.alaska.gov/pubs/id/21961 (last accessed 2016-10-30) (2010).
Silwal, V., 2018. Seismic Moment Tensor Catalog for Crustal Earthquakes in the Cook Inlet and Susitna Region of Southern Alaska. ScholarWorks@UA at http://hdl.handle.net/11122/8383: descriptor file, text file of catalog, figures with waveform fits, and input weight files.
Silwal, V., Tape, C., 2016. Seismic moment tensors and estimated uncertainties in southern Alaska. J. Geophys. Res. Solid Earth 121, 2772–2797. https://doi.org/10.1002/2015JB012588.
Stähler, S.C., Sigloch, K., 2016. Fully probabilistic seismic source inversion — part 2: modelling errors and station covariances. Solid Earth 7, 1521–1536. https://doi.org/10.5194/se-2016-87.
Stanley, R.G., Haeussler, P.J., Benowitz, J.A., Goodman, D.K., Ravn, R.L., Shellenbaum, D.P., Saltus, R.W., Lewis, K.A., Potter, C.J., 2013. New Stratigraphic Revelations in the Subsurface Susitna Basin, South-central Alaska, from Geochronology and Biostratigraphy [poster]: GSA Cordilleran Section Meeting, Fresno, CA, May 22, 2013: Alaska Division of Geological & Geophysical Surveys, 1 sheet. https://doi.org/10.14509/26887.
Storchak, D.A., Di Giacomo, D., Bondár, I., Engdahl, E.R., Harris, J., Lee, W.H.K., Villaseñor, A., Bormann, P., 2013. Public release of the ISC-GEM global instrumental earthquake catalogue (1900–2009). Seismol. Res. Lett. 84 (5), 810–815. https://doi.org/10.1785/0220130034.
Tape, C., Christensen, D., Moore-Driskell, M.M., Sweet, J., Smith, K., 2017. Southern Alaska lithosphere and mantle observation network (SALMON): a seismic experiment covering the active arc by road, boat, plane, and helicopter. Seismol. Res. Lett. 88 (4), 1185–1202. https://doi.org/10.1785/0220160229.
Tape, C., Christensen, D.H., Driskell, M.M., 2015. Southern Alaska Lithosphere and Mantle Observation Network. Other/Seismic Network. https://doi.org/10.7914/SN/ZE_2015.
Tarantola, A., 2005. Inverse Problem Theory and Methods for Model Parameter Estimation. Siam, Philadelphia, Penn., USA.
Trop, J.M., Szuch, D.A., Rioux, M., Blodgett, R.B., 2005. Sedimentology and provenance of the upper Jurassic Naknek formation, Talkeetna Mountains, Alaska: bearings on the accretionary tectonic history of the Wrangellia composite terrane. Geol. Soc. Am. Bull 117 (5/6), 570–588. https://doi.org/10.1130/B25575.1.
Veenstra, E., Christensen, D.H., Abers, G.A., Ferris, A., 2006. Crustal thickness variation in south-central Alaska. Geology 34 (9), 781–784.
Waldhauser, F., Ellsworth, W.L., 2000. A double-difference earthquake location algorithm: method and application to the northern Hayward fault, California. Bull. Seismol. Soc. Am. 90 (6), 1353–1368. https://doi.org/10.1785/0120000006.
Wang, Y., Tape, C., 2014. Seismic velocity structure and anisotropy of the Alaska subduction zone derived from surface wave tomography. J. Geophys. Res. Solid Earth 119, 8845–8865. https://doi.org/10.1002/2014JB011438.
Wéber, Z., 2018. Probabilistic joint inversion of waveforms and polarity data for double-couple focal mechanisms of local earthquakes. Geophys. J. Int. 213, 1586–1598. https://doi.org/10.1093/gji/ggy096.
Wei, M., McGuire, J.J., Richardson, E., 2012. A slow slip event in the south central Alaska Subduction Zone and related seismicity anomaly. Geophys. Res. Lett. 39. https://doi.org/10.1029/2012GL052351.
Wickens, A.J., Hodgson, J.H., 1967. Computer Re-evaluation of Earthquake Mechanism Solutions. Publications of the Dominion Observatory, Vol. 33, No. 1, Ottawa, Canada Department of Energy, Mines, and Resources, Contribution 103 to the International Upper Mantle Project.
Willis, J.B., Haeussler, P.J., Bruhn, R.L., Willis, G.C., 2007. Holocene slip rate for the western segment of the Castle Mountain fault, Alaska. Bull. Seismol. Soc. Am. 97 (3), 1019–1024. https://doi.org/10.1785/0120060109.
Wilson, F.H., Hults, C.P., Schmoll, H.R., Haeussler, P.J., Schmidt, J.M., Yehle, L.A., Labay, K.A., 2009. Preliminary Geologic Map of the Cook Inlet Region, Alaska. In: Open-File Report 2009-1108.
Wood, H.O., Neumann, F., 1931. Modified Mercalli intensity scale of 1931. Bull. Seismol. Soc. Am. 21 (4), 277–283.
Zhang, H., Thurber, C.H., 2003. Double-difference tomography: the method and its application to the Hayward fault, California. Bull. Seismol. Soc. Am. 93 (5), 1875–1889. https://doi.org/10.1785/0120020190.
Zhao, L.S., Helmberger, D.V., 1994. Source estimation from broadband regional seismograms. Bull. Seismol. Soc. Am. 84 (1), 91–104.
Zhu, L., Helmberger, D., 1996. Advancement in source estimation techniques using broadband regional seismograms. Bull. Seismol. Soc. Am. 86 (5), 1634–1641.
Zhu, L., Rivera, L.A., 2002. A note on the dynamic and static displacements from a point source in multilayered media. Geophys. J. Int. 148, 619–627. https://doi.org/10.1046/j.1365-246X.2002.01610.x.